5-2011

Senior Design II Final Report: Red Bull Air Racer

Eric H. Kirchoff
University of Tennessee - Knoxville, ekirchof@utk.edu

Chad Sutton
University of Tennessee - Knoxville

Andrew Kail
University of Tennessee - Knoxville

Sydney Fears
University of Tennessee - Knoxville

Senior Design II Final Report: Red Bull Air Racer

Chad H. Sutton, Eric Kirchoff, Andrew Kail, Sydney Fears
Department of Mechanical, Aerospace and Biomedical Engineering
University of Tennessee, Knoxville, TN, 37916

Submitted to Dr. Robert Bond
May 2, 2011

Abstract

The preliminary design process of modern aircraft is a very important process for aerospace engineers to learn. To expand on previous assignments, this capstone design project aims to be a full and in-depth analysis of the design process. The objective of this project was to design a theoretical, full-scale, pusher configuration air racer capable of competing in the Red Bull Air Race, specifically on the Budapest track.

The design process began by researching the race requirements and many of the flight characteristics of various pusher configuration aircraft. Using the basic requirements for the race and research into previous pusher designs provided a generic model to begin preliminary analysis. With an initial model in place, the aerodynamic profile of the design was the first to be examined along with the selection of the power plant. As the aerodynamic profile of the aircraft was being calculated, the track was also being analyzed so that an estimate of the course run time could be determined. Throughout the process various parameters were changed as the performance analysis was determined. Using the projected flight envelope, a structural analysis of the air racer was performed. The wing structure and material components of the aircraft were determined to satisfy the structural integrity needed for the race maneuvers and to properly meet the required safety factor.

Through the use of the design process, a theoretical, full-scale pusher aircraft was created in hopes of being capable of competing for first place in the Red Bull Air Races. The aircraft was measured to finish the track in 49.2 seconds using a very simple track analysis. Also during the project, a scale model was made using a rapid prototyping stereolithography machine owned and operated by the University providing more accurate aerodynamic data. Using this model, the aerodynamic conditions of the aircraft were not validated to a very high degree of accuracy, but were proved to be relatively accurate.

Table of Contents

Nomenclature

English:

a	- lift curve slope of wing (1/rad)
a_t	- lift curve slope of tail (1/rad)
a_x	- acceleration in x (m/s^2)
a_y	- acceleration in y (m/s^2)
$\bar{c}$	- mean aerodynamic chord (m)
C_p	- coefficient of power
C_y	- chord distribution
D	- propeller diameter (m)
g	-gravity(m/s^2)
GW	- gross weight (N)
I_{Req}	- total required moment of inertia (m^4)
I_{st}	- stringer design moment of inertia (m^4)
I_{xx}	-second mass moment of inertia (m^4)
J	- advance ratio (1/rev)
M_D	- design load moment
M_L	- root moment based on limit load (N/m^2)
n	-load factor
P	- shaft power to propeller (W)
R	-turn radius(m)
SM	- static margin
S_{wet}	-Area of aircraft if completely submerged in water (m^2)
S_{ref}	-Area of the planform of the wings (m^2)
V	- airspeed (m/s)
V_{HT}	- volume of horizontal tail
W_r	- approximation of weight at the root
W_w	-wing weight (N)
x_{acwb}	- distance from nose to aerodynamic center of wing body (m)
x_{cg}	- distance from the nose to the center of gravity (m)
x_n	- distance from the nose to the neutral point (m)

Greek:

ρ	- air density (kg/m^3)
ε	- angle of the engine effective thrust line with respect to the flight path (deg)
λ	- taper ratio
Γ	-streamline
ω	-turn angle (rad)
θ	-flight path angle (rad)
σ_u	-ultimate tensile strength

1. Introduction

THE scope of this project was to design a pusher convention aircraft capable of achieving a competitive runtime in the Red Bull Air-racing league as compared to the general tractor convention models such as the MX-S and the Edge 540 (See Figures 1.1 and 1.2) which are most commonly flown in these races. Typically, pusher aircraft are aerodynamically more efficient and smaller than their equivalent tractor convention brothers because the tapered aft end of the fuselage does not have to extend as far since the aft airflow is all sucked into the propeller stream anyway. The form drag is in turn reduced because the boundary layer of the skin airflow is re-energized upon entrance into the propeller stream. Also, for the purpose of maneuverability pusher aircraft can be superior since in theory, they are less stable than general tractor configuration aircraft. From the point of view of the pilot, forward and downward line of sight is also improved since the engine and propeller are not in the front as an obstruction, which proves very useful when flying low to the ground around tight obstacles.

This design was broken into four main categories for consideration: Aerodynamic, Stability, Structural, and Flight Profile Analysis. A detailed account of these will each be presented, following a brief overview of the preliminary considerations that were quantified.

Figure 1.1: Edge 540

Figure 1.2: MX-S

2. Red Bull Acrobatic Aircraft Design Requirements/Restrictions

The following key rules and regulations were taken from the Red Bull Air Race World Championship Regulations 2010 Edition, information on which can be found below. Due to the scope of this project, not all regulations were substantiated since the design did not mature to the necessary level of detail to do so. However, all of the regulations that apply to work accomplished were successfully met. There were two specific regulations that were ignored in order to make this configuration of aircraft legal. Regulation 6.1 states that each aircraft must have the following general configuration: single engine driving propeller, followed by fixed symmetrical wing, followed by horizontal and vertical tail. In order to accommodate a pusher aircraft, this had to be neglected since the aerodynamic configuration is, for lack of a better word, reversed. Regulation 6.4 states that each aircraft must have fixed landing gear on board. Since this is usually accomplished in a tail dragger fashion (see Figures 1.1 and 1.2 for examples), this regulation also needed to be neglected. A pusher aircraft is equipped with its propeller at the aft end of the plane, and thus in order to have fixed landing gear, there would be substantially more aerodynamic drag induced by the wetted area of the landing gear necessary

for take-off. With the propeller at the aft end of the aircraft, longer gear would have to be used in the rear to allow for ground clearance, and if small landing gear were used in the front, the wings would be at a negative angle of attack thus preventing the aircraft from generating lift. In order to even the playing field concerning aerodynamic drag, a retractable landing gear arm was used in the front of the aircraft.

All other regulations will be discussed in their respective sections including those involving aerodynamic, stability, structural considerations, and flight characteristics. Note that all weights were considered as point loads in the Stability section. Below are the documented rules and regulations from the Red Bull Race Committee.

Technical Definitions
2.1 Mass
- Race Aircraft Mass – Camera Control and Transmission box, Race Fuel, Pilot, Spare Air system, G Race Suit
- Race Pilot Mass – Pilot excluding Helmet, Parachute, and inflatable life vest
- Race Aircraft Empty Mass – Race Aircraft totally empty except for 10 quarts engine oil

Flight Performance
4.1 Load Distribution Limits
- Define Center of Gravity (fixed CG only)
- Static stability analysis
- Pitch and yaw stability/moments
- Structural Limits

4.2 Mass Limits
- Mass not less than 540 kg/ 1190 lb (If less must carry ballast in safe location)
- Assume 50 L fuel
- Telemetry, Cameras and Camera Control Systems 10 kg / 22 lb
- Spare Air System 6 kg / 12 lb

4.3 Stalling Speed
- Shall not exceed 61 knots (70 mph) at max race mass

4.4 Velocity Never Exceed (VNE)
- Define this with the flight envelope

4.5 Take-off Performance
- Take-off distance shall not exceed 500 m at minimum Race Mass

4.6 Landing Performance
- Horizontal distance to come to a stop from 50 feet above landing surface (FAR 23.75)
- At minimum allowable race mass, cannot exceed 500m
- Only wheel brakes can be used to stop plane

Structure

5.1 Limit Maneuvering Load Factors
- Can operate at least +/- 12 g at maximum allowable race mass
- Safety factor of 1.5

5.2 Roll-over Structure
- Located either forward or aft of cockpit
- Able to withstand point load (applied vertically from the top) of 2 times race takeoff mass

5.3 Cockpit Structure
- If manufactured of steel tube, 2 cm of padding around tubes with flame retardant materials
- Avoid Splinter-able materials

5.4 Pylon Impact Case
- Load assumptions made for pylon impact on wing, tail, main landing gear

Design and Construction

6.1 Configuration
- Single engine driving propeller, followed by fixed symmetrical wing, followed by horizontal and vertical tail **(neglected for pusher configuration)**

6.2 Payload
- Should be designed to carry equipment in 9.7.6

6.3 Wingspan
- Between 7 and 8.5 m including wingtips

6.4 Landing Gear
- Fixed Landing Gear Only **(neglected for equality)**
- Minimum wheel size 5"
- Minimum tire size 500 x 5.00 w/ 6 ply
- Heavy duty brake discs minimum thickness 0.250" (no inner wheel brakes)
  - Only approved supplier (Grove and Cleveland)
- Wheel pants minimum ground clearance of 1" with tire inflated

6.5 Seat
- Designed to sit upright, with a recline angle greater than 30 degrees with respect to the thrust line

6.6 Bird Strike Protection
- Air intake screen of max mesh width of 10 mm
- An alternate air intake system shall be fitted. It must supply the engine with air, to run at not less than 18 inches of manifold pressure with the main air intake closed. Alternate air

must be taken from an angle not less than 90° to the longitudinal axis of the Race Aircraft.

Power Plant

7.1 General
- Piston Engine with 6 cylinders or less with max 10:1 compression ratio
- 540 Cylinder Bore 5.125", Stroke 4.375", Displacement 541.5 cu in, Max Bore 0.010" Oversize
- Two Magnetos for ignition only
- Alternator capable of supplying power to aircraft systems and charge battery
- 6 point fuel injection system with nozzles located in standard Lycoming position (no electronic injection)
- Cooling engine with ambient air only
- Piston crown thickness less than 0.250"
- Engine should have 5 hours of operation and data

7.2 Engine Intake Air
- Other than sump breather gases, and fuel for use of combustion, no other mixture can be sprayed into intake air

7.3 Starting the Engine
- Starter motor and battery so pilot can start independently
- Ground power may be used in ground starting

7.4 Fuel
- Aviation Gasoline 100LL according to ASTM D 910 only
- Minimum of 50 L with no means of dumping
- No fuel cooling
- Only ambient air can be used as oxidizer (no turbo or supercharging)

7.5 Inverted Fuel and Oil System
- Capable of sustaining inverted flight for minimum of 30 seconds
- Only inverted oil system approved is Inverted Christen System

Additional Technical Specifications

8.1 Propeller
- Propeller and its governor must comply with the overhaul times listed in Appendix B (6 yrs or 600 hrs)

8.2 Smoke System
- Must produce 2 L/min and must last from smoke on to crossing of finish line
- Must be based on injecting smoke oil into exhaust stream

Payload

10.1 Camera Control and Transmission Box
- Height 19 cm, Width 30 cm, Length 45 cm
- Mass 12.1 kg / 26 lb equipped
- Mounted on luggage rack directly behind pilot

3. Layout & Preliminary Analysis

The first considerations pertained to the initial geometry of the wing section. In order to help locate the aerodynamic center in a desirable spot behind the center of gravity, an aft swept wing body was chosen for this application. Strakes were also implemented on the wings to store the fuel load in an effort to move the center of gravity farther forward and keep it in front of the aerodynamic center. Since most of the aircraft used the Red Bull Races (examples in Figures 1.1 and 1.2 above) are actually manufactured as acrobatic aircraft, they are equipped with symmetric, un-cambered airfoils for the purpose of sustaining inverted flight for certain maneuvers. For the purpose of this design, there was no need for sustained inverted flight longer than a second or two, so a cambered airfoil (NACA 2312) was used for the wing cross-section in order to allow the aircraft to fly at a zero ε and thus reduce the overall induced drag. When an aircraft has symmetric airfoils for inverted flight, it is forced to fly at a slightly pitched upward angle to generate lift, in turn increasing the frontal area of the aircraft. Table 3.1 below gives the resultant dimensions and specifications for the preliminary design of this aircraft. The wing span was required to be between 7 and 8.5 meters wide for safely navigating through the course pylons (referenced in the Flight Profile Analysis section) according to regulation 6.3 as referenced in the Rules/Regulations section (Red Bull Race Committee). To clarify, the Root-Strake Span is the span between the centerline of the aircraft and the end of the strake, while the Strake-Tip Span is the distance from the end of the strake to the wingtip. The Mate Chord refers to the chord of the strake if it were extended to the centerline of the aircraft, and the Strake Chord is the chord length at the transition from strake to main wing frame defined by the Root and Tip Chords. The following equations were used from external sources in the creation of Table 3.1.

$$AR = \frac{b^2}{S}$$ (John D. Anderson 425)   [3.1]

$$\lambda = \frac{c_t}{c_r}$$ (John D. Anderson 423)   [3.2]

$$C_{MAC} = \frac{2}{3} C_r \left(\frac{1+\lambda+\lambda^2}{1+\lambda} \right)$$ (John D. Anderson 428)   [3.3]

$$\tan \Lambda_{LE} = \tan \Lambda_{C/4} + \left[\frac{(1-\lambda)}{AR(1+\lambda)} \right]$$ (Raymer 52)   [3.4]

Table 3.1: Wing Parameters

Wing Geometry					
Wing Span (b)	8.00	m	Sweep LE (Λ_{LE})	26.24	deg
Root-Strake Span	2.50	m	Planform Area (S)	10.00	m^2
Strake-Tip Span	5.50	m	Aspect Ratio (AR)	6.40	
Mate Chord (C_{mate})	2.25	m	Taper Ratio (λ)	0.43	
Root Chord (C_r)	1.75	m	Mean Chord (C_{MAC})	1.32	m
Strake Chord (C_{str})	1.44	m	Airfoil	NACA 2312	
Tip Chord (C_t)	0.75	m			

The canard geometry became the next driving factor since, for safe operation of a pusher aircraft in this configuration these must stall first in order to retain control of the aircraft. If the canards were allowed to stall first, the aircraft would be forced into an unrecoverable stall where the un-stalled canards would hold the nose pitched upward while the plane plunged toward the ground. The associated nose drop effect of the canard stalling before the wing also serves as a warning to the pilot that the plane is beginning to stall, and to take action. The canards were located as far forward as possible in order to allow for the maximum moment arm about the aerodynamic center of the airplane, and as high as possible to prevent the trailing edge streamlines of the airfoil to affect the airflow coming into the leading edge of the wing.

There are a couple of ways to go about ensuring the canards stall first. One of which would be to mount them at slightly higher angle of attack with respect to the wings, causing the canards to hit their maximum lift coefficient at a given angle of attack before the wings. This is assuming similar or identical airfoil characteristics for both the wings and the canards. However, this would mean that by geometry, the frontal projected area of the canards would be slightly higher than necessary (picture a piece of cardboard at zero angle of attack and one at 5 degrees and consider the amount of drag increase). For this reason, an alternate method was chosen. By noting that a more cambered airfoil will generally have a higher lift curve slope, the assumption was made that for a given angle of attack, a higher cambered airfoil would stall first. Thus by using an airfoil with a higher camber, the canards were able to be mounted at zero angle of attack with the wing, while also ensuring that they will stall first. For this reason, the canards were designed with the NACA 4409 airfoil section.

Since this plane is only operating in the subsonic regime and no further center of gravity shift was necessary at this time, a taper ratio (λ) of zero was used. In order to get a feel for the relative size that the canards should be relative to the wings for adequate maneuverability, some typical ratios were studied for typical home-built and acrobatic aircraft. The data presented in Table 3.2 was taken from (Roskam, Airplane Design Part II: Preliminary Configuration Design and Integration of the Propulsion System 191). Note that this method of approximation was also used for the vertical stabilizers, and will be referenced below also. Beginning with the first column and moving to the right, S_h/S_{ref} is the ratio horizontal area of the canards or tail to the reference area of the wing planform, S_e/S_h is the ration of the elevator area to horizontal tail or canard area, x_h is the distance between the neutral points of the canards and wings, V_h is derived from Equation 3.5, and $C_{e\ \%Ch}$ is the elevator chord in percent chord of the canard mean aerodynamic chord. By averaging this data, a good ballpark estimate for the size of the canards

relative to the wing was determined and used to obtain the dimensions in Table 3.3, which gives the specifications for the canard geometry.

$$V_h = (x_h S_h)/(S_{ref} c_h)$$ (Roskam II 191)   [3.5]

Table 3.2: Canard to Wing Ratio Data

Horizontal Tail Volume and Elevator Data					
TYPE	S_h/S_{ref}	S_e/S_h	x_h [m]	V_h	$C_{e\ \%Ch}$
PIK-21	0.1361	0.45	3.08	0.30	0.45
P-70S	0.1871	0.60	2.95	0.44	0.60
SA-III Sequoia	0.1473	0.46	3.32	0.36	0.46
300 Ord-Hume	0.1962	0.43	3.38	0.59	0.43
AVERAGE	**0.1667**	**0.49**	**3.18**	**0.42**	**0.49**

Table 3.3: Canard Parameters

Canard Geometry					
Wing Span (b)	3.25	m	Sweep LE (Λ_{LE})	0.00	deg
Tip Chord (C_t)	0.43	m	Aspect Ratio (AR)	7.56	
Root Chord (C_r)	0.43	m	Taper Ratio (λ)	1.00	
Planform Area (S_h)	1.40	m^2	Mean Chord (C_{MAC})	0.43	m
Airfoil	NACA 4409				

The geometry of the vertical stabilizers was determined in a similar manner to that of the canards. In order to ensure that the plane would have adequate maneuverability, the same aircraft compared above for horizontal tail and canard data were studied for vertical tail and aileron data. Table 3.4 shows this data comparison and the resulting averages from (Roskam, Airplane Design Part II: Preliminary Configuration Design and Integration of the Propulsion System 191). The notation is the same as in Table 3.2 except that the ailerons and vertical tail are referenced. Equation 3.6 was used in the determination of V_v.

$$V_v = (x_v S_v)/(S_{ref} b)$$ (Roskam II 191)   [3.6]

Table 3.4: Vertical Stabilizer to Wing Ratio Data

Vertical Tail Volume, Rudder and Aileron Data					
TYPE	S_v/S_{ref}	S_r/S_v	x_v [m]	V_v	$C_{r\ \%Cv\ root}$
PIK-21	0.0457	0.33	3.20	0.03	0.24
P-70S	0.0563	0.67	3.20	0.03	0.59
SA-III Sequoia	0.0672	0.44	3.23	0.03	0.35
300 Ord-Hume	0.1269	0.31	4.02	0.06	0.27
AVERAGE	**0.0740**	**0.44**	**3.41**	**0.04**	**0.36**

$C_{r\ \%Cv\ tip}$	S_a/S_{ref}	$C_{a\ \%Cw\ in}$	$C_{a\ \%Cw\ out}$	$y_{a\ \%b/2\ in}$	$y_{a\ \%b/2\ out}$
0.49	0.13	0.13	0.13	0.00	1.00
0.76	0.08	0.20	0.20	0.52	0.88
0.68	0.13	0.26	0.26	0.55	1.00
0.43	0.09	0.29	0.29	0.60	0.95
0.59	**0.11**	**0.22**	**0.22**	**0.42**	**0.96**

A symmetric airfoil (NACA 0015) was used for the vertical stabilizers since they need only generate lift when the plane rudders or begins to veer off of straight flight. The root chord is the same as the tip chord of the main wing for mating purposes, and a general 60 degree sweep was used for sportiness and controllability. Table 3.5 presents all of these specifications for the vertical stabilizers.

Table 3.5: Vertical Stabilizer Parameters

Stabilizer Geometry					
Total Span	2.50	m	Sweep .25 (Λ_{25})	60.00	deg
Tip Chord (C_t)	0.30	m	Aspect Ratio (AR)	4.76	
Root Chord (C_r)	0.75	m	Taper Ratio (λ)	0.40	
Planform Area (S_v)	1.31	m^2	Mean Chord (C_{MAC})	0.56	m
Airfoil	NACA 0015				

Figure 3.1 shows the finished wing-strake-stabilizer product with the theoretical wing area shown (neglecting the fuselage interference). The wing strakes were located such that they could carry the fuel load and shift the center of gravity forward for stability. Also, a 5 degree off perpendicular orientation was given to the vertical stabilizers to give a more aesthetically pleasing and sporty look.
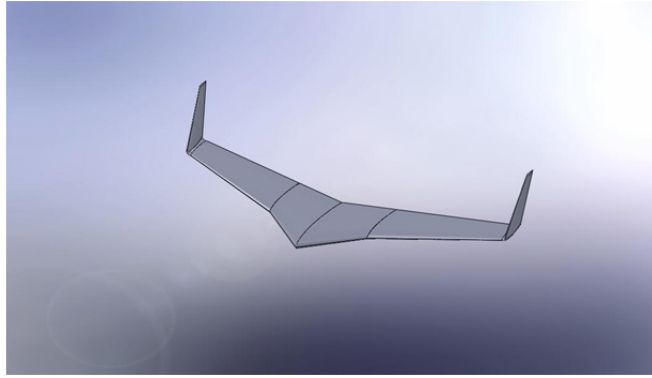
Figure 3.1: Completed Wing Model (Solid-Works)

The fuselage dimensions were constrained by the average pilot size and the size of the engine that was used. The engine will be discussed in further detail section V with the rest of the power plant. Table 3.6 gives the locations of the canard, landing gear, and wing placement relative to the nose of the fuselage, along with the length and width of the fuselage. The wing and canard placement will be discussed in section VII where the stability analysis is presented. The placement of the rear landing gear was determined by the necessary clearance for the rear propeller diameter (2.03 meters) in order to keep in from hitting the ground. The propeller used will also be discussed in section V with the power plant. Figure 3.2 shows the completed model of the fuselage.

Table 3.6: Fuselage Geometry and Mates

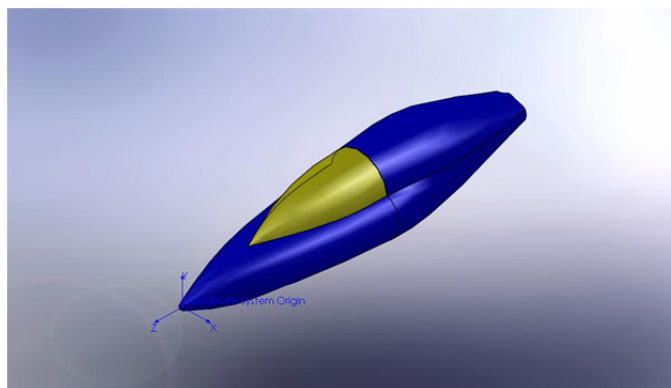| Fuselage Geometry & Mates		
Total Length	5.00	m
Maximum Width	1.25	m
Wing X_{ac} to Nose	3.125	m
Canard X_{ac} to Nose	0.60	m
Rear Landing Gear to Nose	4.00	m

Figure 3.2: Fuselage

The associated stall speeds for the canards and wings in their presented configuration is presented in Figure 3.3 as a function of altitude. It is evident from the plot that the canards will stall before the wings at zero angle of attack, and are given a nice gap of roughly 5 m/s. This verifies that the canards will always stall before the wings since they not only have a higher stall speed, they will also stall first when the plane is at a high angle of attack, as stated before.
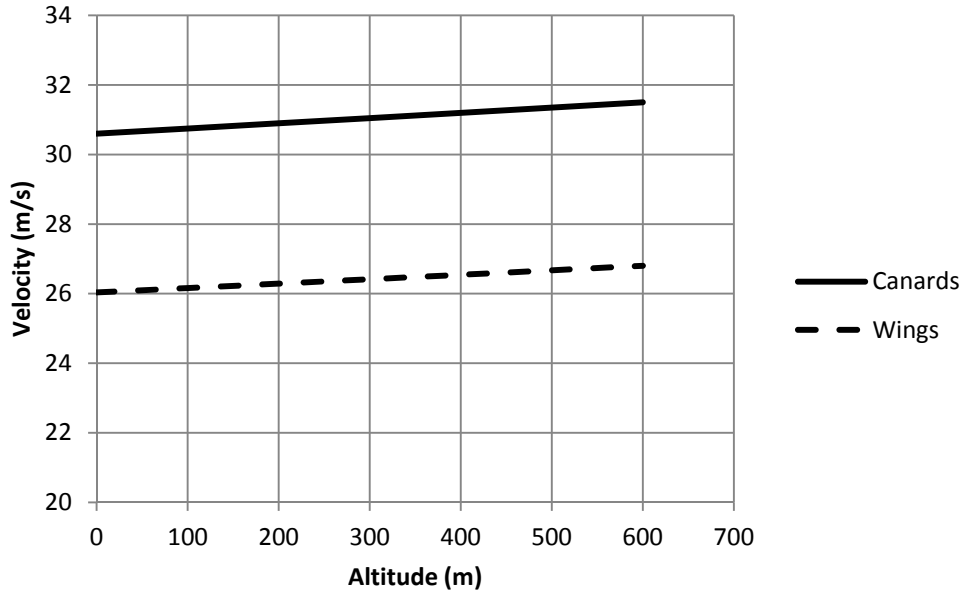

Figure 3.3: Stall Speeds vs. Altitude

Figure 3.3 also shows the compliance with Regulation 4.3, which states that the stall speed shall not exceed 70 mph, which equates to about 31 m/s. The stall speeds were calculated using the following equation from Anderson's *Aircraft Performance and Design* book using standard atmospheric conditions at each respective altitude.

$$V_{stall} = \sqrt{\frac{2}{\rho_\infty} \frac{W}{S} \frac{1}{C_{L\,max}}} \qquad\qquad \text{(John D. Anderson 254)} \qquad [3.7]$$

In equation 3.7, ρ_∞ is the local atmospheric density, W is the weight of the aircraft, S is the planform of the wings, and $C_{L\,max}$ is the maximum lift coefficient of the wing section corrected from the theoretical coefficient for the airfoil.

4. Power Plant

The initial power plant selected for use in the aerobatic pusher aircraft was the Lycoming L/TIO-540-J. This engine has a power output of 350 hp, 261 kW, and weighs 2.4 kN. The main reason for the selection of this engine was foremost its high power output. However, there were several engines with the same power, and from here it was selected for its high power-to-weight ratio. However, after a review of the Red Bull Air Race regulations it was deemed that this engine was illegal for use in the competition because it is turbocharged. Regulation 7.4 states,

"Only ambient air can be used as oxidizer." This required that a new engine had to be selected. The Lycoming AEIO-580-L1B5 was selected as the replacement engine. Table 4.1 displays a list of pertinent engine specifications.

Table 4.1: Engine specifications for the Lycoming AEIO-580-L1B5

Compression Ratio	8.90:1			
Power	320	hp	238624	Watts
RPM	2700	rev/min	45	rev/s
Height	24.46	in	62.13	cm
Width	34.25	in	87.00	cm
Length	40.24	in	102.21	cm
Weight	449	lbs	203.85	kg

Although the AEIO-580 engine has the largest power output of the engines available for use under the Red Bull Air Race rules, it is possible that another engine with less power would perform better. A smaller engine would weigh less and have a smaller displacement. During design, the fuselage had to be remodeled to accommodate the width associated with this engine and the plane is over the minimum allowable weight of 5.3 kN (Regulation 4.2). The best method for determining this would be an iterative approach that encompassed all aspects of the flight performance. This was not done due to time constraints of the project and the need to address other portions of the aircraft. It is sufficient to note that the engine selection would affect the power output, propeller efficiency, structural requirements, drag, lift, etc. Despite the many variables, this engine is believed to perform best for the current needs and therefore has been integrated into the current design.

The MTV-9-B/203-206 propeller has been selected for this aircraft. This is a constant speed, three-bladed propeller. After contacting MT-Propeller and specifying the use, they sent information on two MTV-9 series propellers. Unfortunately, the information provided was in German and had to be translated before use. This resulted in one incorrect calculation for the propeller efficiency. However, after analyzing the data, this error was recognized and corrected. The propeller efficiency data was given in terms the coefficient of power and the advance ratio. The coefficient of power is defined in terms of power input, surrounding air density, revolutions per second, and propeller diameter.

$$C_p = \frac{P}{\rho n^3 D^5} \qquad [4.1]$$

The shaft power to the propeller is assumed to remain constant from the engine and from Table 4.1, P = 24,000 Watts. The air density will change depending on atmospheric conditions, but since the flight will occur at relatively low altitude, Budapest is at 102 m, the flight density is assumed to remain constant at ρ = 1.225 kg/m^3. The angular velocity is also constant from the engine output where n = 45 rev/s. Therefore, the coefficient of power is only a function of the propeller diameter. The advance ratio will also vary with propeller diameter, but it is also a function of the airspeed.

$$J = \frac{V}{nD} \qquad\qquad [4.2]$$

The airspeed will vary throughout the flight and, therefore, is a dependent variable. The propeller diameter is the only variable that can be changed to increase propeller efficiency. However, it is difficult to determine the peak propeller efficiency unless the exact operating conditions are known. For this analysis, the MTV-9-B/203-206 is assumed to have a blade diameter of 2.03 m and the MTV-9-B/198-25 has propeller diameter of 1.98 m. The calculated propeller efficiencies are shown in Figure 4.1. Since the propeller diameter is already determined, the advance ratio could be replaced by an equivalent airspeed. This would allow for a direct correlation between the airspeed and propeller efficiency, but this is unnecessary and not done here. As can be seen in Figure 4.1, the 203-206 has higher propeller efficiencies than the 198-25. For this reason, the MTV-9-B/203-206 was selected as the propeller for this aircraft.
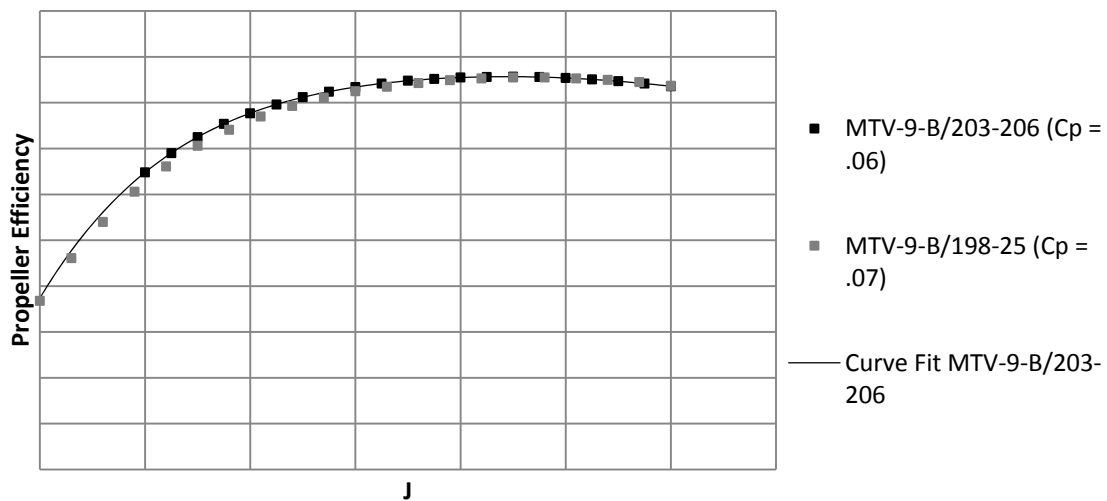

Figure 4.1: Propeller efficiencies versus advance ratio for two MTV-9 series propellers

A curve fit has been applied to this efficiency data to use in calculating the power available from this engine-propeller coupling. It is a sixth degree polynomial that was selected for the close correlation with the data. This is a purely empirical equation that is not based on underlying physical principles. This equation is given as:

$$\eta_{pr} = -0.0839J^6 + 0.7521J^5 - 2.7449J^4 + 5.2849J^3 - 5.9098J^2 + 3.7305J - 0.174 \qquad [4.2]$$

It is important to note that this equation is valid only from $0.2 \leq J \leq 1.4$. Outside this range, there is no data to correlate with and since no underlying physical principle justifies the empirical formula, this equation should not be used.

5.   Aerodynamic Analysis

VLM

The Vortex Lattice Method (VLM) was used during initial aerodynamic analysis to give an estimate for the lift generated by the wing. The VLM is a simple computational method that is capable of generating lift data for a wing of finite size, assuming it as a flat plate at a very low angle of attack. The method works by breaking the wing down into grid sections that each generates a horseshoe vortex. These vortices then induce a velocity upon every other grid section along the entire length of the wing. Summing each of the generated streamlines then gives a simple algebraic equation for the lift as a function of the angle of attack.

The VLM was performed using a MATLAB code written to take into account any adjustments in wing geometry during the design process. The procedure began by assuming the wing dimensions to be input were the wingspan, taper ratio, and quarter chord wing sweep. The file then builds a matrix of control points and boundary points based on the wing dimensions and the desired number of grid sections. Each grid panel has a control point located at the 3 quarter chord point and a boundary point at the port and starboard edges of the panel and is input into the matrix in terms of the wingspan b.

By taking into account the induced vortices and boundary conditions at each panel, a simplified equation for the streamlines produced from one panel to another were simplified into equation 5.1.

$$
W_{m,n} = \frac{\Gamma_n}{4\pi} \left\{ \frac{1}{(x_m-x_{1n})(y_m-y_{2n})-(x_m-x_{2n})(y_m-y_{1n})} \left[\frac{(x_{2n}-x_{1n})(x_m-x_{1n})+(y_{2n}-y_{1n})(y_m-y_{1n})}{\sqrt{(x_m-x_{1n})^2+(y_m-y_{1n})^2}} - \right. \right.
$$

$$
\left. \frac{(x_{2n}-x_{1n})(x_m-x_{2n})+(y_{2n}-y_{1n})(y_m-y_{2n})}{\sqrt{(x_m-x_{2n})^2+(y_m-y_{2n})^2}} \right] + \frac{1.0}{y_{1n}-y_m} \left[1.0 + \frac{x_m-x_{1n}}{\sqrt{(x_m-x_{1n})^2+(y_m-y_{1n})^2}} \right] - \frac{1.0}{y_{1n}-y_m} \left[1.0 + \right.
$$

$$
\left. \left. \frac{x_m-x_{2n}}{\sqrt{(x_m-x_{2n})^2+(y_m-y_{2n})^2}} \right] \right\} \tag{5.1}
$$

The MATLAB code then runs the calculation for each of the panels and builds a matrix where each panel is a function of each streamline with a solution based on the wingspan, free stream velocity, and angle of attack. Using a build in Jacobian Method matrix solver in MATLAB the streamline functions were then calculated. The lift generated by each panel is then integrated then divided by the dynamic pressure and wing planform area to give a linear equation for the coefficient of lift as a function of the angle of attack. Figure 5.1 shows an example of the C_l vs. alpha curve generated by the MATLAB program.
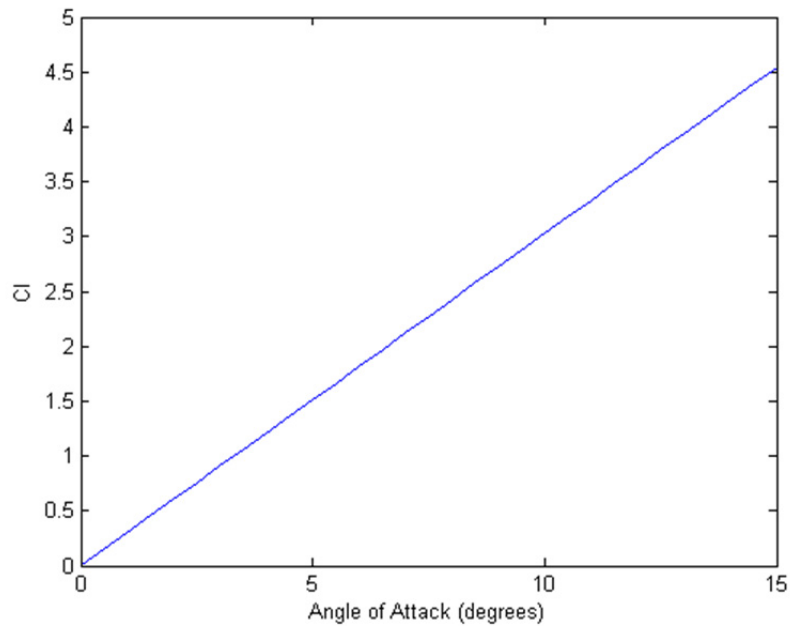
Figure 5.1: Coefficient of lift versus angle of attack calculated using VLM

Also for use in the structural analysis is the need for a lift distribution across the wing. Instead of the program only generating a C_l curve, the also plotted the lift generated along the length of the wing. Figure 5.2 is an example of one such lift curve. In the plot, one may notice the dip or notch in the curve. This dip is due to a part of our wing geometry where the wing is broken down into two wing sections with different wing sweeps and taper ratios.
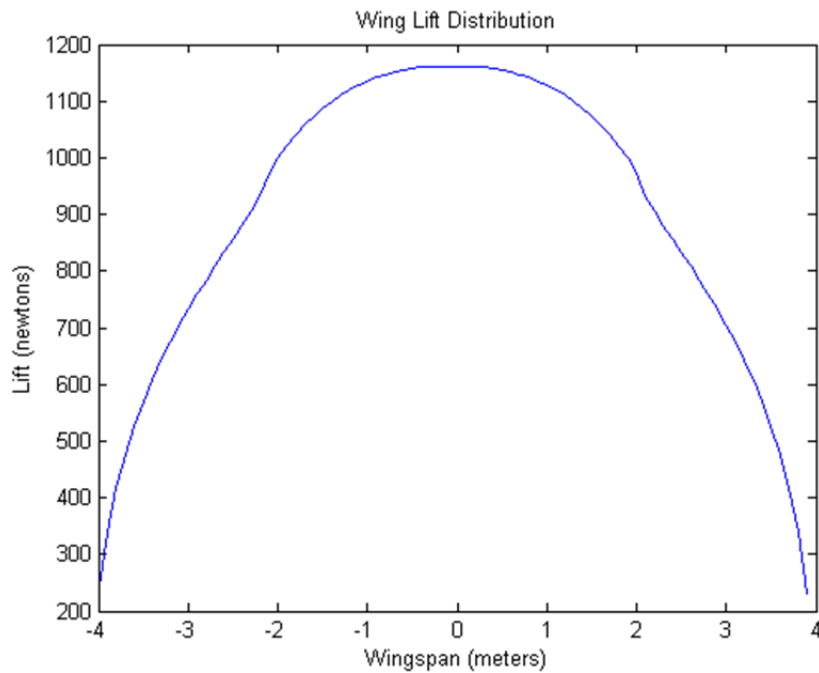

Figure 5.2: Wingspan lift distribution

The Drag Polar

With the preliminary design work and power plant considerations completed, it was now time to quantify an accurate portrayal of the drag polar of this aircraft. The true aerodynamics of aircraft have puzzled engineers since man first took flight in the days of the Wright brothers, leading to the development of many different methods of estimating the drag polar. Given the iterative nature of the design process, it was not possible to dive head first into an intricate analysis of the drag buildup on each component of the airplane since, until the very end, the airplane was still changing form. Thus, three different and increasingly difficult methods of estimating the drag polar of this aircraft will be discussed and employed in this section.

The first method used in developing a working representation of the drag polar entailed estimation based on other aircraft, and had almost no dependency on the actual geometry of the aircraft. This method employed the basic definition of the drag polar in its simplest form for any arbitrary aircraft, and is shown in Equation 5.3 below.

$$C_D = C_{Do} + KC_L^2 \qquad \text{(John D. Anderson 130)} \qquad [5.3]$$

The zero-lift drag C_{Do} in this equation was first quantified using Figure 2.54 and 2.55 of *Aircraft Performance and Design* on page 128 and 129 (Reference found in Bibliography). Figure 2.54 gives the S_{wet}/S_{ref} ratio versus the wing loading W/S_{ref} for several different aircraft that are currently or have been in practice. Figure 2.55 gives the skin friction coefficient C_{fe} as a function of the Reynolds Number for several different aircraft. The decision was made to use values roughly between those of a Cessna Skyplane and an F-104, since that is probably a good estimate of where a subsonic racing aricraft would reside. By employing Equation 5.3 below, the first zero-lift drag estimate was obtained. Note that the S_{ref} factor is in this case the projected area of the fuselage if viewed head on.

$$C_{Do} = \frac{S_{wet}}{S_{ref}} C_{fe} \qquad \text{(John D. Anderson 128)} \qquad [5.3]$$

In order to quantify the K factor in Equation 5.2, a relation including a parameter called the span efficiency factor *e* and the aspect ratio of the aircraft *AR* was used, given in Equation 5.4. The span efficiency factor is used to account for the non-elliptical lift distribution along the span of the wing.

$$K = \frac{1}{\pi e AR} \qquad \text{(John D. Anderson 129)} \qquad [5.4]$$

By defining a string of values for the lift coefficient and plugging the values from Equations 5.3 and 5.4 into Equation 5.2, a preliminary depiction of the drag polar was generated and is shown at the end of this section in Figure 5.2.

After some progressive maturing of the design to the point of pre-defined components, a new more in depth analytical approach was taken to generate a more accurate depiction of the resulting drag polar. This method has been referred to in many different reference texts as "The Component Build-up Method" and basically does just that, build a drag polar representation by

analyzing all of the different components individually, and then putting them all together. Unfortunately, this is not a direct additive method. For reasons that are still unexplained, when the drag for a wing and a fuselage are analyzed separately and then together, there is always a higher amount of drag in the latter case. For this reason, a number of interference factors will be employed throughout this method to correct for this phenomenon.

The entire section to follow is related to the component drag on the wings and was all pulled from *Airplane Design: Part IV* in section 4.2. This reference will be needed to make use of any charts referenced in this section. The wing drag coefficient in its simplest form is given by Equation 5.4 below with the total drag coefficient C_{Dw}, the zero-lift drag C_{Dow}, and the drag due to lift C_{DLw}.

$$C_{Dw} = C_{Dow} + C_{DLw} \quad [5.5]$$

In order to quantify the variables in this equation, several graphical approximations were used from this reference. The wing drag due to lift, as well as all other drag due to lift variables were quantified using the same method as before since the design had not matured to the point of being able to use this method. At this point in the design, this was sufficiently accurate. The equation for each variable will be given, followed by a brief explanation of the variables involved.

$$C_{Dow} = R_{WF}R_{LS}C_{fw}\left[1 + L'\left({}^t/_c\right) + 100({}^t/_c)^4\right]\frac{S_{wet}}{S_{ref}} \quad [5.6]$$

Equation 5.6 gives the relationship for the wing zero-lift drag parameter in Equation 5.5. The wing-fuselage interference factor R_{WF} was obtained using Figure 4.1 in the reference text, which gives a representation of R_{WF} versus the fuselage Reynolds Number for different flight speeds. The lifting surface correction factor R_{LS} was obtained using Figure 4.2 in the reference text, which gives a representation of R_{LS} versus $\cos \Lambda_{(t/c)max}$ where $\Lambda_{(t/c)max}$ is the sweep angle at the maximum value of airfoil thickness over chord length. The turbulent flat plate skin-friction coefficient of the wing C_{FW} was obtained from Figure 4.3 in the reference text, which gives a representation of C_{FW} versus the Reynolds Number calculated using the mean geometric chord of the exposed wing surface. Note, this is not the equivalent trapezoidal wing mean geometric chord used in the preliminary design calculations; this is excluding the wing area that would theoretically pass through the fuselage. The airfoil thickness location parameter *L'* was obtained from Figure 4.4 in the reference text, which gave different values based on where the value of *(t/c)max* is located. The thickness ratio *(t/c)* is defined at the mean geometric chord of the exposed wing.

The entire section to follow is related to the component drag on the fuselage and was all pulled from *Airplane Design: Part IV* in section 4.3. This reference is needed to make use of any charts referenced in this section. The fuselage drag coefficient in its simplest form is given by Equation 5.5 also, where the zero-lift drag C_{Do} and the drag due to lift C_{DL} are substituted with the fuselage values. In order to quantify the variables in this equation, several graphical approximations were used from this reference. The equation for each variable will be given, followed by a brief explanation of the variables involved.

$$C_{Dof} = R_{WF}C_{ff}\left[1 + {60}\middle/{(l_f/d_f)^3} + 0.0025\,{l_f}\middle/{d_f}\right]\frac{S_{wet}}{S_{ref}} + C_{Db} \quad [5.7]$$

Equation 5.7 gives the relationship for the fuselage zero-lift drag parameter in Equation 5.5. The wing-fuselage interference factor R_{WF} was obtained using Figure 4.1 in the reference text, which gives a representation of R_{WF} versus the fuselage Reynolds Number for different flight speeds. Since the flow over a fuselage is almost always turbulent (except in special cases where they are specifically designed for laminar flow), the turbulent flat plate skin-friction coefficient C_{ff} was used from Figure 4.3 referenced above. The Reynolds Number for this figure was calculated using the length of the fuselage. The maximum length of the fuselage is l_f and the maximum diameter of the fuselage is d_f. The fuselage base drag coefficient C_{Db} is given by Equation 5.8 below.

$$C_{Dbfus} = \left[0.029\left(\frac{d_b}{d_f}\right)^3 \middle/ \left\{C_{Do_{fus-base}}(S_{wet}/S_{fus})\right\}^{1/2}\right]\frac{S_{wet}}{S_{fus}} \quad [5.8]$$

The fuselage base diameter d_b was obtained from Figure 4.17 in the reference material, which defines it as the equivalent diameter of the cross-sectional area of the rear most section of the fuselage. The zero-lift drag coefficient of the fuselage exclusive of the base C_{Dbfus} as determined from the first term on the right hand side of Equation 5.7.

The entire section to follow is related to the component drag on the empennages and was all pulled from *Airplane Design: Part IV* in section 4.4. This reference is needed to make use of any charts referenced in this section. The empennage drag coefficients in their simplest form are given by Equation 5.5 also, where the zero-lift drag C_{Do} and the drag due to lift C_{DL} are substituted with the empennage values. In order to quantify the variables in this equation, several graphical approximations were used from this reference. Each empennage had its own version of Equation 5.5. The zero-lift drag portion of Equation 5.5 was taken from Equation 5.6 for the wing and replaced with the necessary variables for the empennages. The empennages included the canards and vertical stabilizers.

The entire section to follow is related to the component drag on the landing gear and was all pulled from *Airplane Design: Part IV* in section 4.7. This reference is needed to make use of any charts referenced in this section. The landing gear drag coefficient in its simplest form is given by Equation 5.9 below. In order to quantify the variables in this equation, several graphical approximations were used from this reference.

$$C_{Dgear} = (C_{Do_{gear}} + PC_L)\frac{S_{gear}}{S_{wet}} \quad [5.9]$$

The zero-lift drag coefficient of the landing gear is based on the reference area of the landing gear, or the projected area of one wheel. This is defined in Figures 4.54-4.60 of the reference material from empirical data on different landing gear configurations. P is a factor that accounts for the variation of gear drag with lift. Figure 4.61 of the reference text gives a method for determining this factor by comparison with other configurations of landing gear. Landing gear design is an art in itself, so with the available time for this project it was not a huge consideration.

After all predictions had been run and a reasonable estimate for the drag polar had been quantified, the use of a new age and cheap modeling technology (Stereolithography) was used to generate a solid-body model for use in wind tunnel testing. Stereolithography is an additive manufacturing process using a vat of liquid UV-curable photopolymer "resin" and a UV laser to build parts a layer at a time. Because of the limitations with the structural integrity of this material, the model had to be made sufficiently large enough such that the smallest structural point of the model was larger than 2 mm, yet still fit in the wind tunnel. However, in giving the model these dimensions, it became too large for the building area of the Stereolithography machine. In order to remedy this problem, the plane had to be sectioned into different tongue and slot parts to be assembled after construction. Figures 5.3, 5.4, and 5.5 show the parts in their un-assembled fashion.
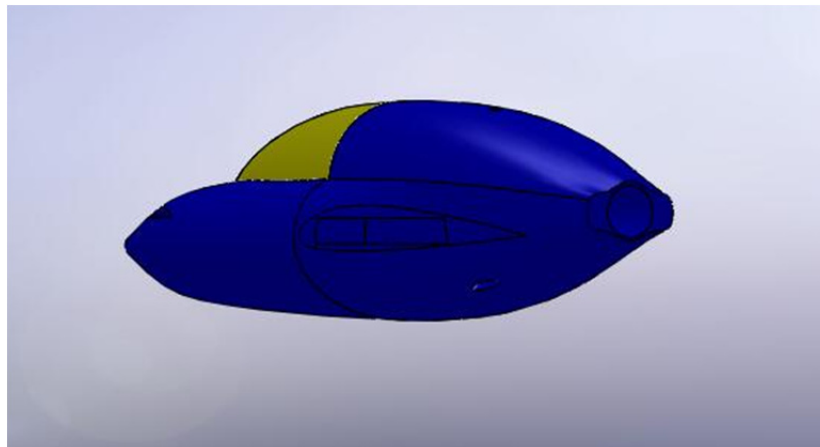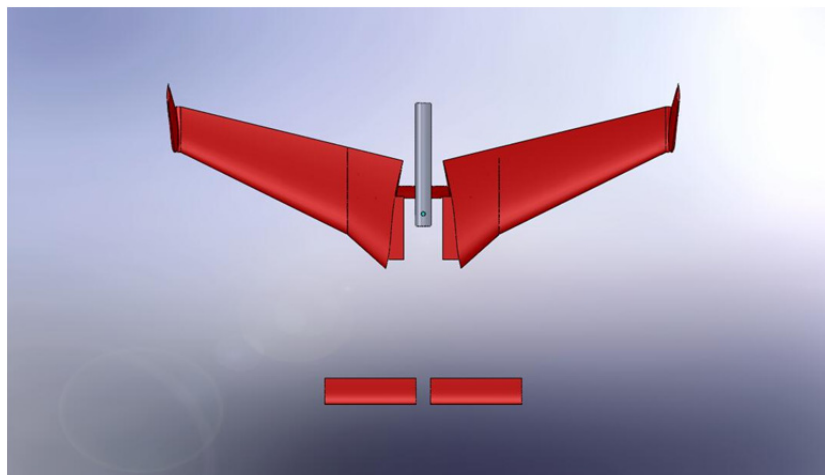

Figure 5.3: Slotted Fuselage

Figure 5.4: Tongue Parts Top View

Figure 5.5: Tongue Parts Front View

It can be seen from the figures that the wings, canards, landing gear, and aluminum mount (will be discussed below) are all made to fit into their corresponding slots in the fuselage shown in Figure 5.3. In order to adapt the Stereolithography model to the wind tunnel, an aluminum mount had to be fabricated from a standard aluminum rod and plug. The plug was used to narrow the inside diameter of the rod down to the close tolerance needed to fit snugly on the tip of the probe. A set screw was tapped into this location to secure the model in place. Figure 5.6 shows the configuration and specs of the aluminum mounting rod. It can be seen from the figure the shape of the mounting probe of the wind tunnel described above by the dotted outline of the interior of the aluminum mounting rod.
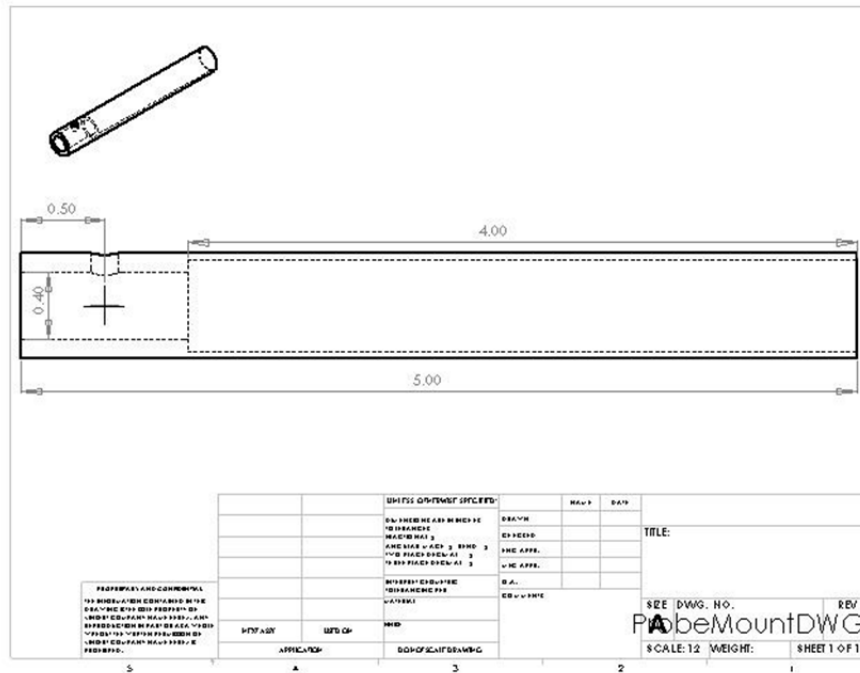

Figure 5.6: Aluminum Mounting Rod

After running several wind tunnel tests on the model at 50 mph from an angle of attack of plus or minus 15 degrees, the comparisons in Figure 5.7 were generated. The legend is made of acronyms for simplicity that stand for Airplane Performance Method (Method 1), Airplane Design Method (Method 2), and the Wind Tunnel Method respectively. The wind tunnel output data in the form of lift and drag forces, so in order to reduce the data to lift and drag coefficients for use in the drag polar comparison, Equations 5.10 and 5.11 were used.

$$D = q_{\infty} S_{ref} C_D \quad [5.10]$$

$$L = q_{\infty} S_{ref} C_L \quad [5.11]$$

Unfortunately, while the predictions made from Methods 1 and 2 are very close to one another, the data obtained from the wind tunnel testing produced significantly higher drag forces. This could be attributed to the higher amount of skin friction that was caused by surface roughness on the model than would be expected of a polished metallic fuselage. Also, this fuselage was designed to have the aft airflow entering into the propeller stream, and thus reducing the form drag on the aircraft at that point. The wind tunnel model did not have a propeller, thus this could have also caused a percentage of the higher drag readings. Overall, the drag data from the wind tunnel test was relatively close to the empirical predictions made earlier in this section.
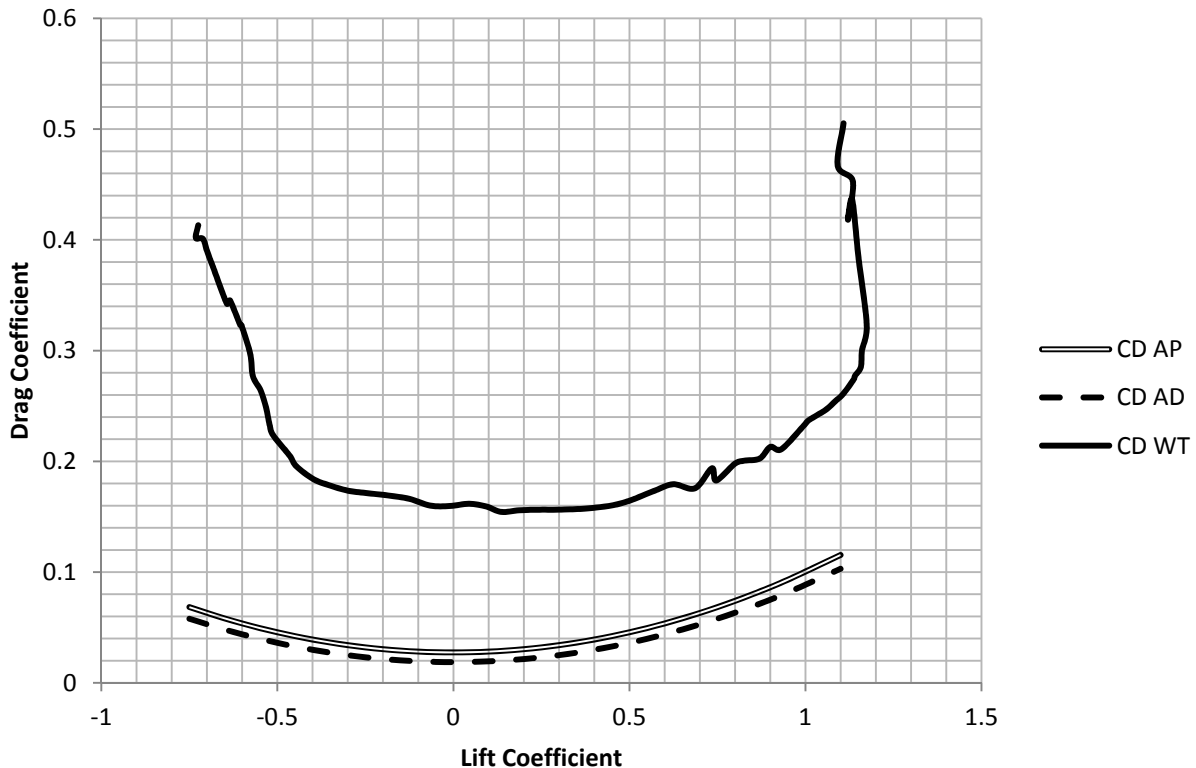

Figure 5.7: Comparison of the drag polar via different methods discussed

6.   Weight Estimation

To begin structural and stability analyses, a preliminary weight balance was necessary. This was done by using a class one method for weight estimation described by Dr. Jan Roskam in *Airplane Design Part V: Component Weight Estimation*. This was a five step process that began by making a list of important weight parameters and making some initial design weight choices and estimations as is displayed in Table 6.1. Most of the values in this table were known already or simply estimated such as the crew weight. It was known that the plane would be a single seat aircraft; therefore, an average weight of group members was used. As this was only an initial step, it could become more specific later.

Table 6.1: Step 1 for determining estimated weight of aircraft and aircraft components

		mass (kg)	weight (N)
Gross Take-Off Weight	W_{TO}	550	5396
Empty Weight	W_E	425	4167
Mission Fuel Weight	W_F	43	424
Payload Weight	W_{PL}	18	178
Crew Weight	W_{crew}	82	804
Trapped Fuel and Oil Weight	W_{tfo}	5	49
Flight Design Gross Weight	GW	550	5396

Step 2 in determining the aircraft and aircraft component weights was to identify a category and airplanes in that category that could be compared to the airplane being designed. Initially the category was homebuilt propeller driven aircraft, but the only plane in this category was a Bede BD5B. This plane only has a 30 kW engine and therefore is not comparable to our design goal. The next group selected was the single engine propeller driven aircraft. There were several planes in this category. Only three were selected for comparison however. These three were the Beech J-35, Saab Safir, and Rockwell 112TCA. They were chosen mostly for engine size, but these all had at least two seats and were significantly heavier than our design goal. The main difference however was that they were all tractor pull aircraft. There was no pusher configuration, so this could not be avoided.

Steps 3 and 4 were to list the significant component weights that applied to the aircraft being designed and find what percentage of the gross weight this represented in the aircraft selected for comparison. These were then averaged together. This process is shown in Table 6.2. Any category that is left blank did not have specific data available. The most important part of this estimation is the structure weight. The power plant weight is already set and the fixed equipment for the plane that was being designed is minimal.

Table 6.2: Steps 3 and 4 for estimating aircraft and aircraft component weights

			Beech J-35	Saab Safir	Rockwell 11	Average
I. Structure Weight		W_{struct}	0.312	0.316	0.366	0.331
	Rear Wing	Wing Grp/GW	0.131	0.104	0.113	0.116
	Canard	Empenn. Grp/GW	0.02	0.023	0.033	0.025
	Fuselage	Fuselage Grp./GW	0.069	0.145	0.121	0.112
	Langing Gear	Landing Grp/GW	0.021		0.045	0.033
	a. Nose Gear					
	b. Rear Gear					
II. Power Plant Weight		W_{pwr}	0.201		0.189	0.195
	Engine					
	Propeller					
	Fuel System					
III. Fixed Equipment Weight		W_{feq}	0.115		0.151	0.133
	Flight Control System					
	Hydraulic System					
	Electrical System					
	Instrumentation					

The last step for determining preliminary weight estimations was to multiply the design gross weight of our aircraft times the average of the component weights from steps 3 and 4. This gave numbers for a first weight approximation. These were then adjusted based on reasonable assumptions. For example the wing mass was increased by 10 kg because it would likely need more structural stability due to high g-loading and the equipment mass was decreased by 35 kg because there is only one seat and not as many fixtures in an airplane designed to compete in the Red Bull Air Races. Table 6.3 shows this step. As you can see in this table, the final weight estimate using a class one method predicts a takeoff gross weight of 5.5 kN. This is very close to the flight design gross weight given in step 1 and was likely to change as more specific analyses of the various components were undertaken.

Table 6.3: Step 5 of preliminary weight estimation

Componet	First Weight Estimate		Adjustment		Why	Final Weight Estimate	
Wing	62.6 kg	614.5 N	10 kg		Structural support	72.6 kg	712.6 N
Empennage (including Canard	13.7 kg	134.2 N	5 kg		Structural support	18.7 kg	183.3 N
Fuselage	60.3 kg	591.5 N	0 kg		Structural support/One Seat Width	60.3 kg	591.5 N
Landing Gear	17.8 kg	174.8 N	-10 kg		Smaller Wheels/not full retract	7.8 kg	76.7 N
Power Plant	105.3 kg	1033.0 N	127.4 kg		Known engine weight	232.7 kg	2282.9 N
Fixed Equipment	71.8 kg	704.6 N	-35 kg		Less seats/Less Equipment	36.8 kg	361.2 N
Empty Weight	331.6 kg	3252.6 N				429.0 kg	4208.2 N
Payload	6.0 kg	58.9 N				6.0 kg	58.9 N
Crew	82.0 kg	804.4 N				82.0 kg	804.4 N
Fuel	43.3 kg	424.8 N				43.3 kg	424.8 N
Trapped Fuel and Oil	3.0 kg	29.4 N				3.0 kg	29.4 N
Takeoff Gross Weight	465.9	4570.1 N				563.3 kg	5525.7 N

7.   Stability Analysis

The stability analysis performed for our model was a simple longitudinal stability analysis. A more detailed approach was started, but this was deemed inappropriate due to the many estimations and unknowns that were being used in the model. This technique is taken from *Aircraft Performance and Design* by John D. Anderson. The output of the stability analysis is in static margin. This is defined as the distance from the neutral point to the center of gravity over the mean aerodynamic chord of the main wing structure.

$$SM = \frac{x_n - x_{cg}}{\bar{c}}$$
    (John D. Anderson 444)   [7.1]

For most aerobatic aircraft, the static margin is very low which means that the neutral point and the center of gravity are located very close together. This is generally assumed to be around 5% for an aerobatic aircraft. A positive static margin has the center of gravity located in front neutral point for an airplane. The first step in calculating the static margin is by finding the center of gravity of the airplane. This was done by using the weight estimation made in section 5 and selecting component locations according to the initial design of our model and geometric constraints. It is necessary that this be variable in the beginning stages to ensure that the plane is stable. The next step is to calculate the neutral point of the aircraft. This accounts for the lift of the main wing body and the tail.

$$x_n = x_{acwb} + V_{HT}\left(\frac{a_t}{a}\right)$$
    (John D. Anderson 444)   [7.2]

For conventional aircraft, the tail volume is positive and will shift the neutral point further back along the plane, but for a canard, the neutral point is shifted forward (Stengel).

After both the neutral point and center of gravity are calculated, the static margin can be adjusted by moving the wings and canards fore and aft, adjusting the wing and canard planform area, and changing the weight distribution of the aircraft. It was simple enough to create a design that achieved a static margin of about 5% $\bar{c}$; however, this configuration made the canard stall speed lower than the main wing stall speed. This is unacceptable for canard aircraft because a stall on the back wing will result in a nose up reaction that will cause a loss of control for the aircraft. If the canard stalls first, the plane will go nose down, increasing the speed and therefore recovering from the stall.

The stability analysis was not performed until late in the design process for this aircraft. This should have been done much earlier to avoid making significant changes to the design. If only the weight distribution is varied, the minimum static margin achievable while maintaining the proper stall characteristics is about 69% $\bar{c}$. This means that the plane will be overly stable and sluggish to the controls. For this case, Table 7.1 displays the pertinent information. This is the aircraft configuration that has been modeled for flight performance. Changes were not made because a wind tunnel model was produced to obtain flight data.

Table 7.1: Stability and stall information for modeled aircraft

x_{cg}	3.1	m
x_n	4.0	m
SM	69.0	%
$V_{stall,canard}$	26.9	m/s
$V_{stall,wing}$	26.0	m/s

By altering the geometry and weight distribution of the aircraft, a static margin of about 12 % $\bar{c}$ is possible with the proper stall characteristics. However, this does require radical changes in the geometry and weight distribution. Specifically, the wing taper ratio had to be decrease, the wing had to be moved slightly forward along the fuselage, the canard was moved forward along the fuselage, and the canard chord length was decreased. In future considerations, the stability of the aircraft should be considered sooner, and this should be extended to calculating control surface sizing and forces.

8.   Structural Analysis

Basic structural analysis is a critical part of the conceptual design process of the Red Bull racer, thus the loads that would be sustained during flight of the aircraft would have to be determined. The load determination would require a combination of aerodynamics using the span-wise lift distribution, structures, and known and estimated weights. A calculation of the shear and moment distribution along the wing would be necessary to reach a more specific conclusion about material selection and analysis of geometric cross sections that could be used as structural components within the wing of the aircraft. The focus of the structural analysis would be the main wings of the aircraft due to the high-g loads that must be sustained during the flight profile. The wing weight, fuel load, and lift distribution would be the primary concern for the shear and bending moments that would be calculated about the wing. An Excel program would be created to aid in the structural analysis.

The first part of the structural design process consisted of setting the limit load factor, n. This would be very important for the design scope of the structural analysis of the aircraft due to the extreme loads the aerobatic racer would experience during flight. It was initially assumed that the load factor should be set at n=6, being the upper limit of general aviation aerobatic aircrafts; however, the aircraft was allowed to operate at a maximum of +/- 12 g at allowable race mass (Regulation 5.1). A conclusion was reached that the limit load should be set at the highest operational limit prescribed by the race regulations at n=+/-12. The positive limit load would be the primary emphasis due to the particular maneuvers during the flight profile being that the structural analysis would be based on the critical case of the pull-up during the loop when the aircraft load factor could be at as high as n=+12.

The wing structural weight distribution could then be estimated based on the determined load factor. One wing was estimated to be 72.6 kg or 712.2 N based on weight approximations discussed in the weights section of the report. The length of one wing would be half of the wing

span, thus 4m would be the span of one wing. Using the wing geometry defined in the aerodynamics section, the wing was non-elliptical, tapering in both chord and thickness. Thus, it was reasonable to assume the weight distribution to be parabolic. Equation 8.1 was used to describe the wing weight where the weight at the root could be approximated by Equation 8.2. The chord distribution could then be derived by Equation 8.3. The wing was not designed to have any geometric or aerodynamic twist thus assuming a trapezoidal wing was reasonable. An Excel program was created to graphically determine a polynomial curve-fit for the graph of the wing weight with respect to the wing length from to root to tip. The wing weight along the wing length was multiplied by 12 to determine the distributive load under the critical case of the loop maneuver at n=12. (See Figure 8.1)

$$W_y = W_r \left(C_y / C_r \right)^2 \qquad\qquad [8.1]$$

$$W_r = 6 * W_w / \left(b \left(1 + \lambda + \lambda^2 \right) \right) \qquad\qquad [8.2]$$

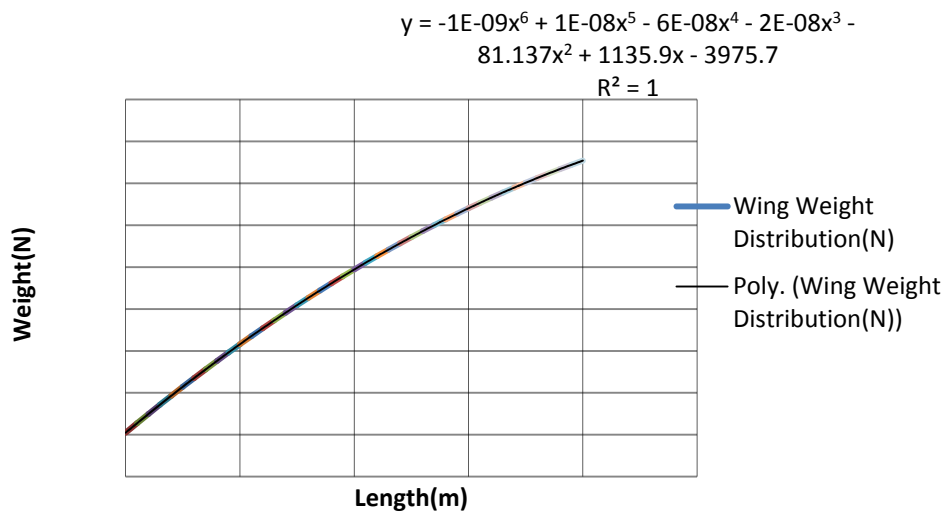$$C_y = C_r \left[1 - 2y/b \left(1 - \lambda \right) \right] \qquad\qquad [8.3]$$

Figure 8.1: Wing Weight Distribution at n=12

The estimation of the fuel load distribution was determined by analysis of the volume of fuel that would be carried and how the fuel would be placed within the wing. It was desired to fit the amount fuel used within the volume of the stake of the wing. The minimum amount of fuel that could be used during the race was 50 liters. (Regulation 4.2.2) This would mean that 25 liters of fuel must be carried in each wing. It was decided that a high octane, general aviation fuel would be used, thus 100LL AvGas at 5.64 lb/gal was chosen. An estimation of the volume of the strake compared to the volume of fuel desired would be necessary. Based on the geometry of the NACA 2312 airfoil, the maximum volume of the strake was calculated by the trapezoid area of the section multiplied by the thickness of the smaller chord of the airfoil section to derive a minimum volume of the strake. The minimum volume of the strake was calculated to be approximately 0.34452 m^3. The volume required for the minimum amount of fuel of 25 liters of

100LL AvGas for one wing was calculated to be 0.025 m^3; thus the strake volume housed enough space for the desired amount of fuel. A parabolic load force was desired for the fuel load distribution so that the force would vary quadratically along the strake's length. This would allow the fuel load to be zero at both the wing root and the strake's end with the maximum load of the fuel at the middle of the strake. A polynomial curve-fit was created to graphically represent a parabolic fuel load within the desired strake distance.(See Figure 2) The chord length of the strake began at 1.75m to 1.44m, with the corresponding values of wing span distance being from 0m to 1.25m. The maximum weight of the fuel based on the minimum volume of fuel of 25 liters per wing was calculated to be 165.49 N. This maximum weight was located at 0.625m from the wing root at the middle of the strake being the minimum of the parabolic load distribution.
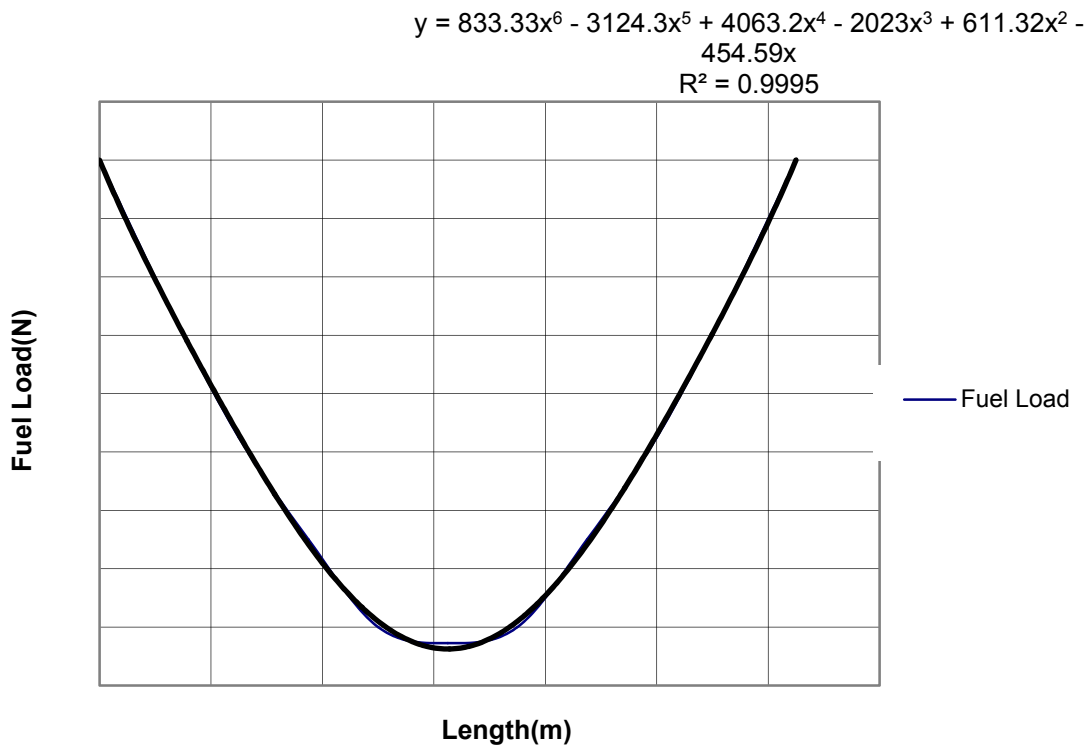
$$y = 833.33x^6 - 3124.3x^5 + 4063.2x^4 - 2023x^3 + 611.32x^2 - 454.59x$$
$$R^2 = 0.9995$$

Figure 2: Fuel Load determination Curve-fit

The lift distribution along the wingspan was determined by the Vortex Lattice method. Details from the usage of the Vortex Lattice method in the aerodynamic profile section were input into the Excel program to graph the spanwise streamline distribution of one wing with respect to the wing length from the root to the tip. A polynomial curve-fit was derived from the graphical data. (See Figure 8.3) Using Equation 8.4, the streamline profile could be used to find the lift force distribution along the wing as a function of the angle of attack, α. It was assumed that the lift produced by the aerobatic racer at n=12 must be greater than or equal to the weight of the aircraft at 12g during the loop maneuver. Thus, 12 times the estimated weight of the aircraft was used as a gauge to ensure that the theoretical lift was great enough to sustain flight at that flight regime.

For the total lift produced by the aerobatic racer to be in reasonable range, the lift could be adjusted as a function of the angle of attack. An angle of attack at 4.902º provided the necessary lift to offset the weight of the aerobatic aircraft at an instant when the weight of the entire aircraft is 12 times that of normal. The lift produced at each increasing distance away from the root of the wing is added to acquire the total contributing lift of one wing at 12g.
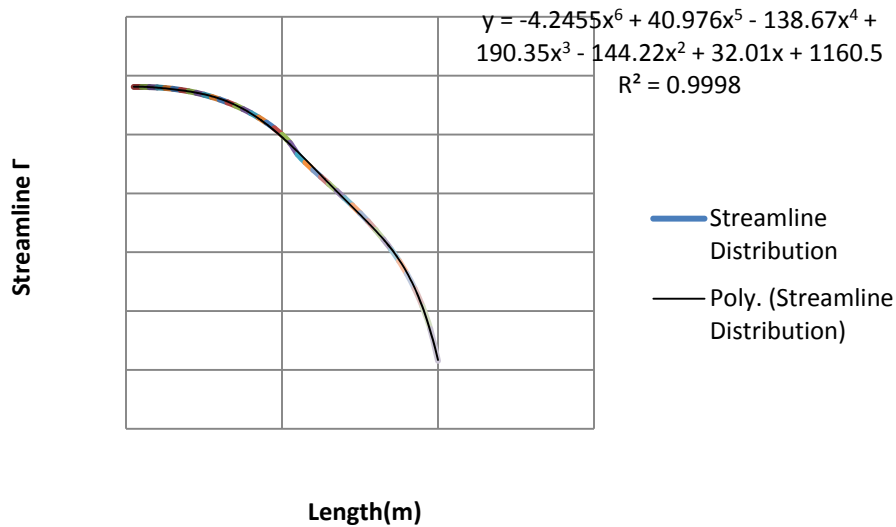

$y = -4.2455x^6 + 40.976x^5 - 138.67x^4 + 190.35x^3 - 144.22x^2 + 32.01x + 1160.5$
$R^2 = 0.9998$

Streamline Distribution

Poly. (Streamline Distribution)

Streamline Γ

Length(m)

Figure 8.3: Streamline distribution along one wing

$$L = \Gamma * V_{max}^2 * \pi^2 * \alpha / 45 \hspace{3cm} [8.4]$$

After the distributed loads of the wing weight, lift distribution, and fuel were determined, the shear and bending moments could be constructed. The Excel program was used to graphically display the shear diagrams for the loads with respect to the wing length. (See Figure 8.4) The shear is given by the sum of the vertical loads along the wingspan by each particular load distribution. The bending moments of each load distribution were then found by integrating the load diagram to find the moment as a function of span location at a load factor of n=12, all moments being equal to zero at the wing root. (See Figure 8.5) Multiplying the bending moment of a distributed load by an arbitrary distance away from the root would give the total shear force of that distributed load at that point. The landing gear weights and locations could be neglected in the shear and moment diagrams due to the fact that the tricycle landing gear would be mounted on the fuselage. The consideration of a wing load due to a wing-mounted engine could also be neglected due to the fact that the engine would be mounted in a pusher configuration at the back of the fuselage.
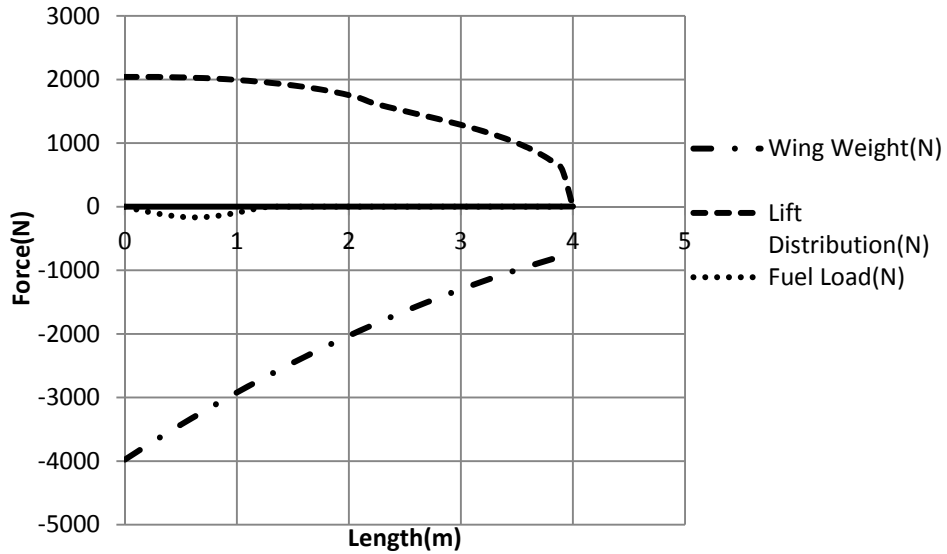
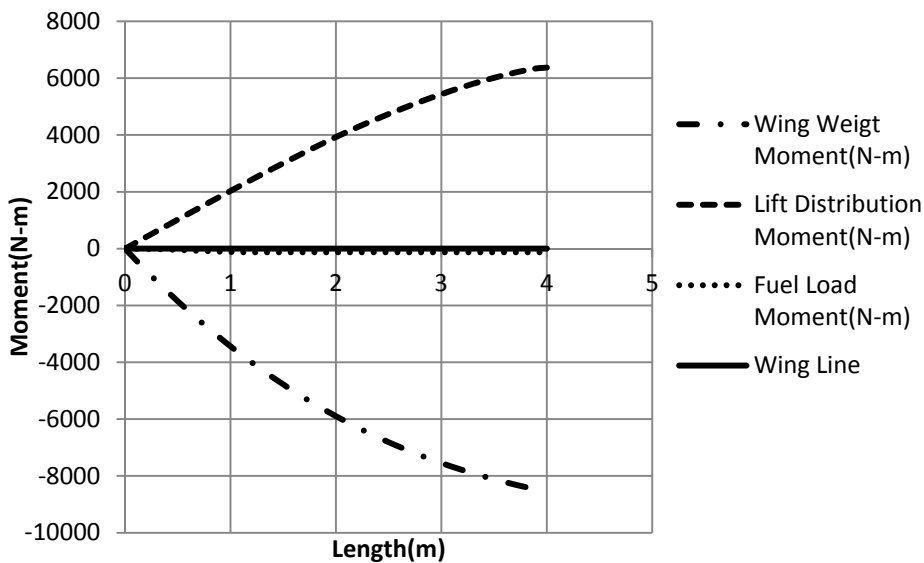**Figure 4: Load Diagram of Wing weight, Lift Distribution, and Fuel at n=12**

**Figure 5: Moment Diagram of Wing weight, Lift Distribution, and Fuel Load at n=12**

After the shear and bending diagrams were created, the moment based on the limit load could be derived. The moment at the root of the wing was zero, but as the distance from the root increased, the sum of the moments of the wing weight, lift distribution, and fuel load reached a maximum magnitude, M_L, of 2304.78 N/m at the tip of the wing. This moment would be critical in the selection of materials and the analysis of structural components used within the wing. The wing strength was required to have a safety factor of 1.5. (Regulation 5.1.2) The design moment, M_D, based on safety factor would be M_L times 1.5, which was calculated to be a magnitude of 3457.18 N/m. (See Equation 8.5) The design load moment would be the critical factor in the selection of the appropriate materials for the structural supports within the wing and the wing skin material.

$$M_D=M_L*\text{safety factor} \qquad\qquad [8.5]$$

The selection of the material for the construction of the wing to support the design moment was based on materials with high strength-to-weight ratios. The material selection would be centered about distinct structural components including: a main and rear wing spar, four stringers, and the wing skin. Materials such as aluminum alloys, steel, carbon fiber, and fiber glass-epoxy were considered for the internal structures of the wing. Due to the fact that cost was not a prominent design parameter, specific aluminum alloys and carbon fiber were decided as the primary materials that would be used in for the wing spars, wing skin, and stringers that would support the loads of the wing. Aluminum is one of the most widely used aircraft materials, and one of the most commonly used aluminum alloys is 2024. 2024 has a density of 2780 kg/m^3 and an ultimate stress, σ_u, of 469 MPa; however a less dense aluminum alloy 6061 was chosen for the wing spars. 6061 had a lower density of 2700 kg/m^3 with an ultimate stress, σ_u, of 310 MPa. This material was thought to be light enough to conserve the weight of the spars within the wing while having the strength to support the bending moment. Aluminum alloy 5086 with even a lower density of 2660 kg/m^3 was chosen as the material for the stringers. 5086 was found to have an ultimate stress, σ_u, of 270 MPa. The stringers within the wing would require the support of a much smaller percentage of the design moment, thus the lighter 5086 was chosen. Carbon fiber was chosen as the material for the wing skin and the control surfaces of the wing. If the spars and stringers using the aluminum alloys were properly designed to support the design moment, the skin load is less critical; however, carbon fiber was chosen because it is very low weight with a very high tensile strength. The carbon fiber used would have ultimate stress, σ_u, of 5650 MPa and a density of 1750 kg/m^3. This would provide more than adequate support for the skin load during the flight profile; all while conserving weight without the loss of tensile strength.

The main and rear wing spar would be the primary concern for the internal structure of the wing. These spars would have to endure most of the load from the design moment. The spars would be represented as a typical geometric shape of an I-beam. The I-beam shape is a symmetrical cross section in which the centroid, C, is located at the intersection of the two axes of symmetry, and therefore coincides with the mid-point of the web. Furthermore, the bending moment is applied to the beam section in a vertical plane so that the *x* axis becomes the neutral axis of the beam section. (See Figure 8.6) The second moment of inertia, I_{xx} must be calculated about this axis. To determine the second moment of inertia I_{xx} of the I-beam, the cross section was considered a block with two pieces removed; however since the I-beam was symmetrical with respect to the *x* axis, the component of the centroid of the blocks is offset equally above or below the x axis. The resulting equation to solve for I_{xx} of the I-beam was derived as $I_{xx} = (BH^3/12)-(*bh^3/12)$, where $*b=B-b$. (See Equation 8.6)
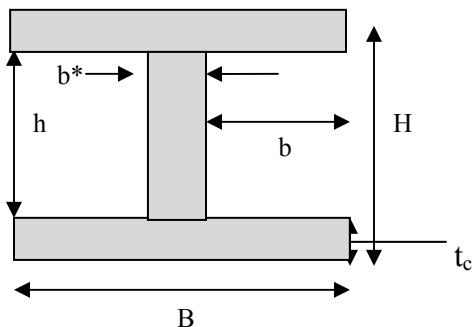
B=width
H=height
h=height of central webbing
b=width of the empty space
b*=width of central webbing=B-b
t_c=thickness of spar cap=(H-h)/2
C=centroid of cross section

Figure 8.6: Schematic I-Beam and dimensions

$$I_{xx}= (BH^3/12)-(*bh^3/12); \quad *b=B-b \qquad\qquad [8.6]$$

Equation 8.7, $I_{Req}= (M_D/\sigma_u)*(t_{max}/2)$, was used to begin the initial steps in the wing spar analysis. This equation represented the total required moment of inertia. T_{max} was set to the maximum thickness of the wing, which would be the maximum thickness of the NACA2312 airfoil. T_{max} would thus be the maximum height, H, of the wing spar plus the wing skin thickness. The total required moment I_{Req} was calculated to be 8.1557E-05. The main spar was decided to be placed at 30% chord since the maximum thickness of the airfoil would be at this location. This would require that moment of the I-beam, I_{xx}, be equal to 60% of the total required moment I_{Req}. The Excel program was used to compute a trial and error analysis based on the thickness of the spar caps, the maximum height of the spar, the spar cap width, the height of the central webbing, and the width of the central webbing. The thickness of the airfoil skin was set to 0.003m; thus any arbitrary spar would be constrained by a maximum height between the thickness of both the airfoil and the thickness of the NACA 2312 airfoil at 12% of the chord. At 30% chord, the concluded dimensions of the main spar can be seen in Table 8.1. The same trial and error analysis was done for the rear spar, which was designed to support 15% of the total required moment at 70% chord. This would require a much smaller spar; however, the spar cap width was designed to be the same as that of the main spar to conserve weight. The dimensions of the rear spar can be seen in Table 8.2. The values of B and b were used as inputs that would affect the different dimensions of the I-beam in order to reach a moment of inertia that met the required moment of the system. The thickness of the spar caps, t_c, were equal to (H-h)/2. (See Figure 8.6) It was noticed that the value of B had more of an impact on the moment of inertia of the spar. This may be so due to the fact that the cross-sectional area of the shear web is less significant compared to the area of the spar caps, being that the spar caps absorb most of the bending force.

Table 8.1: Main Spar Dimensions

B	0.08976m
H	0.2438m
*b	0.03826m
b	0.0515m
h	0.2033m
t_c	0.02023m

Table 8.2: Rear Spar Dimensions

B	0.08976m
H	0.1169m
*b	0.01921m
b	0.07054m
h	0.1107m
t_c	0.003085m

The component design for the stringers was similar; however, the moment of inertia of the stringer shape could be neglected, and the stringer area, A_n and its distance from the bending center, h_n, could be used to find the moment of inertia needed. It was decided that four stringers would be designed to sustain 15% load division of the total required moment. Based on the geometry of the wing, the bending center was found to be at half of the wing span where the chord was 1.25 m. Equation (8.7) was used in the Excel program in a trial and error analysis to calculate the total moment of four stringers with 1ft or 0.3048 m separation between them. In order for the total moment required to be equal to the sum of the moment of inertia of the four stringers, each stringer had to have a diameter of 10.37 mm.

$$I_{Req} = (M_D/\sigma_u)*(t_{max}/2) \qquad [8.7]$$

The last part of the structural analysis consisted of the estimated load division through the skin of the wing. 10% of the load division remained to be distributed in the skin load. With the spars being designed to endure most of the load distribution, the skin of the aircraft was considered a rectangular area, with a length of 4m, a width of 1.25m, and a thickness of 0.003m. Using Equation (8.8) to solve for a design moment, M_D, based on the moment of inertia of the rectangular area, it was found that the carbon fiber material could support a design moment on the order of 1000 times more than the design moment derived based on the limit load. It was concluded that carbon fiber would be highly sufficient in supporting the skin load as well as being used for the control surfaces on the wings.

$$I_{st} = \sum A_n h_n^2 \qquad [8.8]$$

9. Flight Profile Analysis

In order to get an estimate for the vehicles run time on the track, another MATLAB program was written. The track was broken down into several segments of different types. The first type was the straight sections of the track. In this section of the track we assumed the aircraft was flying through accelerated level flight. The second section of track was the turns, where we once again assumed level flight and also constant turning velocity. The final section type is the loop and is the most complex. By breaking down track into these 3 types made it easier to write code that can be duplicated for each section.

Using the map in Figure 9.1 we began to determine how best to break down the track and what methods would be best for gaining an accurate representation analytically. Through trial and error we broke the track down into different sized turns and straightaways. The main objective was to try and maintain a fluid path throughout the track and not introduce any unnecessary sharp turns. Once the track was properly broken down, measurement was needed. Because the track layout was found as a simple image, there were no "rulers" to scale the image to real life. Instead, the distance between the pylons was used as a reference to scale the image up. The pylons are approximately 18-20 meters apart from the center of the pylon.
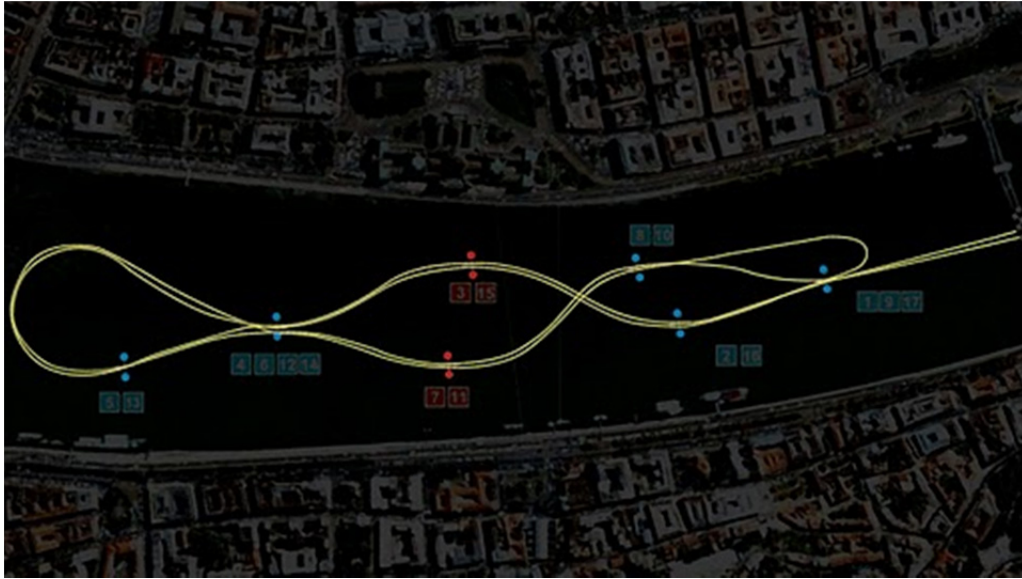

Figure 9.1: Budapest track layout.

With a scale in place the dimensions of the map could be laid out. The track was separated in 16 distinct sections: 10 turns, 3 straightaways, and 3 loops. The straightaways were simple to measure and ranged from 70 meters to 130 meters in length. The turns though were much harder to measure. A compass was used on each turn to empirically match an arch to each of the turn section. Using the curves drawn on the track image, it was possible to measure the dimensions of each turn: the turn radius and the chord length of the turn. The turn radius of each turn, based on a specified load factor, gives the approximate value for the flight speed through the turn and is based on equation 9.1 below.

$$R = \frac{V_\infty^2}{g\sqrt{n-1}}$$ [9.1]

The chord length also gives the turn angle using the law of cosines (equation 9.2).

$$\omega = \arccos\left(\frac{a^2+b^2-c^2}{4ab}\right)$$ [9.2]

Combining the turning angle with the radius gives the arc length which can then be used with the velocity to determine the time of travel along each turn segment.

When accounting for accelerated flight along the straight paths of the track functions were written take into account the variation in drag based on the variation in lift. As the racer accelerates, the angle of attack varies to reduce the lift as the velocity increases and the lift must remain constant during level flight. To account for the changing aerodynamics at each time segment, the coefficients of lift and drag are recalculated and using a force balance as in figure # resulting in equation 9.3.

$$a_x = \frac{(T-D)}{mass} \qquad\qquad [9.3]$$

From there a Taylor series was expanded to calculate the velocity and the location where the velocity is:

$$v_{i+1} = v_i + a_x \cdot \Delta t \qquad\qquad [9.4]$$

and the position is then

$$x_{i+1} = x_i + v_i \cdot \Delta t + \frac{a_x \cdot \Delta t}{2} \qquad\qquad [9.5]$$

Using time steps the position and subsequent velocity along the straight path was then calculated.

The third and most complex segment of the track is the loop, which is broken down into 3 sections. The first section is the actual loop where the vehicle becomes inverted. To account for the change in the coefficient of lift as the ailerons are adjusted, a constant coefficient of lift is assumed based on an assumed load factor. This can be taken as holding the "stick" back at a constant position and the ailerons remain fixed throughout the loop.

Balancing the forces in the perpendicular direction of the loop through equation 9.6 the instantaneous turn radius is calculated.

$$R = \frac{(mass \cdot V_\infty^2)}{(L - W \cdot Cos(\theta))} \qquad\qquad [9.6]$$

After determining the turn radius, the program then begins breaking down the changes in positions and flight path angle. The change in the x and y direction simple are functions of velocity and flight path angle as shown in equations 9.9 and 9.10. Also varying is the path angle and velocity represented below also.

$$\Delta x = V_\infty Cos(\theta)\Delta t \qquad\qquad [9.7]$$

$$\Delta xy = V_\infty Sin(\theta)\Delta t \qquad\qquad [9.8]$$

$$\Delta\theta = \left(\frac{V_\infty}{R}\right)\Delta t \qquad\qquad [9.9]$$

$$\Delta V = \left(\frac{\Delta t}{mass}\right)(T - D - W \cdot Sin(\theta)) \qquad\qquad [9.10]$$

When calculating the change in velocity only the forces in the tangential direction were taken into account as it is assumed to be an instant time step.

The loop program terminates after a specific flight path angle is reached. In this case the program stops at a 5/8ths loop but has been adjusted by small amounts to improve flight time. Following the loop, a line is drawn between the end of the loop and the proceeding pylon in the course. This line has a designated length and angle from which the final path will be taken. This descent path is at an angle and takes into account accelerated flight so a force balance in the x and y direction was performed. The results are equations 9.11 and 9.11.

$$\varSigma F_x = Cos(\beta)(T - D) + Sin(\beta)L \qquad\qquad [9.11]$$

$$\varSigma F_y = Cos(\beta)L - Sin(\beta)(T - D) - W \qquad\qquad [9.12]$$

Dividing the forces by the mass gives the acceleration in each direction and summing the accelerations gives the total acceleration along the flight path. Using another expanded Taylor series the path was broken up into several times steps and was set to terminate upon reaching the final pylon.

10. Conclusion

In retrospect, this has been an overview of the conceptual and preliminary detailed design of a pusher configuration air racer for the purpose of competition in the Red Bull Air Races. First research of the race requirements and many of the flight characteristics of various pusher configuration aircraft was performed. With the use of the basic requirements for the race and research into previous pusher designs, a generic model was developed to begin preliminary analysis. With an initial model in place, the aerodynamic profile of the design was the first to be examined followed by the selection of the power plant. With the aerodynamic profile of the design base-lined, the drag polar was estimated using progressively more in-depth methods. As the aerodynamic profile of the aircraft was maturing in design, the flight profile of the racetrack was also being analyzed so that an estimate of the course run time could be determined. Using the projected flight envelope, a structural analysis of the air racer was performed. The wing structure and material components of the aircraft were determined to satisfy the structural integrity needed for the race maneuvers and to properly meet the required safety factor.

Through the use of the design process, a theoretical, full-scale pusher aircraft was created in hopes of being capable of competing for first place in the Red Bull Air Races. The aircraft was measured to finish the track in 49.2 seconds using a very simple track analysis. Also during the project, a scale model was made using a rapid prototyping Stereolithography machine owned and operated by the University providing more accurate aerodynamic data. Using this model, the aerodynamic conditions of the aircraft were not validated to a very high degree of accuracy, but were proved to be relatively accurate.

11. Works Cited

John D. Anderson, J. (1999). *Aircraft Performance and Design.* Singapore: McGraw-Hill Companies, Inc.

Megson, T. (2007). *Aircraft Structures for Engineering Students 4th Edition.* Burlington, MA .

Raymer, D. P. (2006). *Aircraft Design: A Conceptual Approach 4th Edition.* Reston, Virginia: American Institute of Aeronautics and Astronautics, Inc.

Red Bull Race Committee. (2010). *Regulations Part E: Technical Regulations.*

Roskam, D. J. (1989). *Airplane Design Part II: Preliminary Configuration Design and Integration of the Propulsion System.* Lawrence, Kansas: Roskam Aviation and Engineering Corporation.

Roskam, D. J. (2000). *Airplane Design Part VI: Preliminary Calculation of Aerodynamic, Thrust and Power Characteristics.* Lawrence, Kansas: DARcorporation.

Stengel, R. (2010). *Configuration of Power Effects on Flight Stability.*

12. Appendix

Appendix A: Flight Profile

```
clc
clear all

%Flight Profile program
%Senior Design - Spring 2011
%Andrew Kail, Sydney Fears, Eric Kirchoff, Chad Sutton
%May 2nd, 2011


S=10; %Planform area
W=5396; %Initial Weight
rho=1.225; %Density
g=9.81; %Gravity
t=0;
dt=0.1; %time interval
mass=W/g;
vstart=100; % starting speed
Pa=238624; %power available should change with the introduction of prop data
k=0;
```

A. Straight 1 - Entry

```
s1=160; %meters

v0=vstart;
xs=0;

while xs < s1
  q=0.5*rho*v0^2;
  Cl=W/(q*S);
  Cd=drag(Cl); %drag function
  ax=(Pa/v0-Cd*q*S)/mass; %drag is a function of Cl
  xs=xs+v0*dt+ax*dt^2/2;
  v0=v0+ax*dt;
  k=k+1;
end

t=t+k*dt;
```

B. Right Turn #1

```
r1=180; c1=200; %meters
bank1=80; %degrees
loc1=acos((c1^2-2*r1^2)./(-2*r1^2));
arc1=loc1*r1;
bank1=bank1*pi()/180;
liftt1=W./cos(bank1);
n=liftt1/W;
Vbank1=sqrt(r1*g*sqrt(n^2-1));
ta1=arc1/Vbank1;

t=t+ta1;
```

C. Left Turn #2

```
r2=172.5; c2=215; %meters
bank2=80; %degrees
loc2=acos((c2^2-2*r2^2)./(-2*r2^2));
arc2=loc2*r2;
bank2=bank2*pi()/180;
liftt2=W./cos(bank2);
n=liftt2/W;
Vbank2=sqrt(r2*g*sqrt(n^2-1));
ta2=arc2/Vbank2;

t=t+ta2;
```

D. Straight 2

```
s2=130; %meters

v0=Vbank2;
xs=0; k=0;

while xs < s2
 q=0.5*rho*v0^2;
 Cl=W/(q*S);
 Cd=drag(Cl); %drag function
 ax=(Pa/v0-Cd*q*S)/mass; %drag is a function of Cl
 xs=xs+v0*dt+ax*dt^2/2;
 v0=v0+ax*dt;
 k=k+1;
end

t=t+k*dt;
```

E. Loop 1

```
ptp1=130; %distance between pylons

dt=0.01;
q=0.5*rho*v0^2; %use velocity from previous program segment
n=10; %this is the initial load factor for the loop.  must change eventually
Lloop=n*W;
Clloop=Lloop./(q*S);
Cdloop=drag(Cl);

theta0=0; x=0; y=0; k=0;

while theta0 < (5/8*2*pi())
 q=0.5*rho*v0^2;
 L=q*S*Clloop;
 D=q*S*Cdloop;
 T=Pa/v0;
 n=Lloop/W;

 r=(mass*(v0^2))/(Lloop-W*cos(theta0));
 x=x+(v0*cos(theta0))*dt;
 y=y+v0*sin(theta0)*dt;
 dv=(dt/mass)*(T-D-W*sin(theta0));
 dtheta=(v0/r)*dt;
 v0=v0+dv;
```

```
      theta0=theta0+dtheta;
      k=k+1;
      flight(k,1:5)=[k*dt x y theta0 v0];
    end

    desx=ptp1+x; desy=y;
    beta=atan(y/x);
    line=sqrt(desx^2+desy^2); l=line;

    while l > 0
       q=0.5*rho*v0^2;
       Clfall=0.15;
       L=q*S*Clfall;
       Cdfall=drag(Clfall);
       D=q*S*Cdfall;
       T=Pa/v0;
       ay=(cos(beta)*L+sin(beta)*(D-T)-W)/mass;
       ax=(cos(beta)*(T-D)+sin(beta)*L)/mass;
       v0=v0+sqrt(ax^2+ay^2)*dt;
       line=line-v0*dt; l=line;
       k=k+1;
       flight(k,1:5)=[k*dt x y theta0 v0];
    end

    t=t+k*dt;
```

F. Straight 3

```
    s3=70; %meters

    v0=vstart;
    xs=0;

    while xs < s3
      q=0.5*rho*v0^2;
      Cl=W/(q*S);
      Cd=drag(Cl); %drag function
      ax=(Pa/v0-Cd*q*S)/mass; %drag is a function of Cl
      xs=xs+v0*dt+ax*dt^2/2;
      v0=v0+ax*dt;
      k=k+1;
    end

    t=t+k*dt;
```

G. Left Turn #3

```
    r3=150; c3=180; %meters
    bank3=80; %degrees
    loc3=acos((c3^2-2*r3^2)./(-2*r3^2));
    arc3=loc3*r3;
    bank3=bank3*pi()/180;
    liftt3=W./cos(bank3);
    n=liftt3/W;
    Vbank3=sqrt(r3*g*sqrt(n^2-1));
    ta3=arc3/Vbank3;

    t=t+ta3;
```

H. Right Turn #4

```
r4=165; c4=200; %meters
bank4=80; %degrees
loc4=acos((c4^2-2*r4^2)./(-2*r4^2));
arc4=loc4*r4;
bank4=bank4*pi()/180;
liftt4=W./cos(bank4);
n=liftt4/W;
Vbank4=sqrt(r4*g*sqrt(n^2-1));
ta4=arc4/Vbank4;

t=t+ta4;
```

I. Loop 2

```
ptp2=147.5; %distance between pylons

dt=0.01;
q=0.5*rho*v0^2; %use velocity from previous program segment
n=10; %this is the initial load factor for the loop.  must change eventually
Lloop=n*W;
Clloop=Lloop./(q*S);
Cdloop=drag(Cl);
theta0=0; x=0; y=0; k=0;

while theta0 < (5/8*2*pi()) % Because  the is a 5/8ths loops its goes to far during the pull up manuever.  Instead, my right a for
loop to adjust for the loop
                % distance because its not working well.
  q=0.5*rho*v0^2;
  L=q*S*Clloop;
  D=q*S*Cdloop;
  T=Pa/v0;
  n=Lloop/W;

  r=(mass*(v0^2))/(Lloop-W*cos(theta0));
  x=x+(v0*cos(theta0))*dt;
  y=y+v0*sin(theta0)*dt;
  dv=(dt/mass)*(T-D-W*sin(theta0));
  dtheta=(v0/r)*dt;
  v0=v0+dv;
  theta0=theta0+dtheta;
  k=k+1;
  flight(k,1:5)=[k*dt x y theta0 v0];
end

ptp2=130;
desx=ptp2+x; desy=y;
beta=atan(y/x);
line=sqrt(desx^2+desy^2); l=line;

while l > 0
   %Drag and lift variables are missing!!
   q=0.5*rho*v0^2;
   Clfall=0.15;
   L=q*S*Clfall;
   Cdfall=drag(Clfall);
   D=q*S*Cdfall;
   T=Pa/v0;
   ay=(cos(beta)*L+sin(beta)*(D-T)-W)/mass;
   ax=(cos(beta)*(T-D)+sin(beta)*L)/mass;
```

```
        v0=v0+sqrt(ax^2+ay^2)*dt;
        line=line-v0*dt; l=line;
        k=k+1;
        flight(k,1:5)=[k*dt x y theta0 v0];
    end

    t=t+k*dt;
```

J. Left Turn #5

```
        r5=165; c5=50;
        bank5=80; %degrees
        loc5=acos((c5^2-2*r5^2)./(-2*r5^2));
        arc5=loc5*r5;
        bank5=bank5*pi()/180;
        liftt5=W./cos(bank5);
        n=liftt5/W;
        Vbank5=sqrt(r5*g*sqrt(n^2-1));
        ta5=arc5/Vbank5;

        t=t+ta5;
```

K. Right Turn #6

```
        r6=150; c6=180; %meters
        bank6=80; %degrees
        loc6=acos((c6^2-2*r6^2)./(-2*r6^2));
        arc6=loc6*r6;
        bank6=bank6*pi()/180;
        liftt6=W./cos(bank6);
        n=liftt6/W;
        Vbank6=sqrt(r6*g*sqrt(n^2-1));
        ta6=arc6/Vbank6;

        t=t+ta6;
```

L. Straight 4

```
        s4=70;

        v0=vstart;
        xs=0;

        while xs < s4
         q=0.5*rho*v0^2;
         Cl=W/(q*S);
         Cd=drag(Cl); %drag function
         ax=(Pa/v0-Cd*q*S)/mass; %drag is a function of Cl
         xs=xs+v0*dt+ax*dt^2/2;
         v0=v0+ax*dt;
         k=k+1;
        end

        t=t+k*dt;
```

M. Left Turn #7

```
        r7=237.5; c7=130;
        bank7=80; %degrees
        loc7=acos((c7^2-2*r7^2)./(-2*r7^2));
```

```
arc7=loc7*r7;
bank7=bank7*pi()/180;
liftt7=W./cos(bank7);
n=liftt7/W;
Vbank7=sqrt(r7*g*sqrt(n^2-1));
ta7=arc7/Vbank7;


t=t+ta7;
```

N. Loop 3

```
ptp3=130; %distance between pylons
dt=0.01;
q=0.5*rho*v0^2; %use velocity from previous program segment
n=10; %this is the initial load factor for the loop.
Lloop=n*W;
Clloop=Lloop./(q*S);
Cdloop=drag(Cl);
theta0=0; x=0; y=0; k=0;

while theta0 < (5/8*2*pi())
 q=0.5*rho*v0^2;
 L=q*S*Clloop;
 D=q*S*Cdloop;
 T=Pa/v0;
 n=Lloop/W;

 r=(mass*(v0^2))/(Lloop-W*cos(theta0));
 x=x+(v0*cos(theta0))*dt;
 y=y+v0*sin(theta0)*dt;
 dv=(dt/mass)*(T-D-W*sin(theta0));
 dtheta=(v0/r)*dt;
 v0=v0+dv;
 theta0=theta0+dtheta;
 k=k+1;
 flight(k,1:5)=[k*dt x y theta0 v0];
end

ptp2=130;
desx=ptp2+x; desy=y;
beta=atan(y/x);
line=sqrt(desx^2+desy^2); l=line;

while l > 0
   q=0.5*rho*v0^2;
   Clfall=0.15;
   L=q*S*Clfall;
   Cdfall=drag(Clfall);
   D=q*S*Cdfall;
   T=Pa/v0;
   ay=(cos(beta)*L+sin(beta)*(D-T)-W)/mass;
   ax=(cos(beta)*(T-D)+sin(beta)*L)/mass;
   v0=v0+sqrt(ax^2+ay^2)*dt;
   line=line-v0*dt; l=line;
   k=k+1;
   flight(k,1:5)=[k*dt x y theta0 v0];
end

t=t+k*dt;
```

O. Left Turn #8

```
r8=150; c8=75;
bank8=80; %degrees
loc8=acos((c8^2-2*r8^2)./(-2*r8^2));
arc8=loc8*r8;
bank8=bank8*pi()/180;
liftt8=W./cos(bank8);
n=liftt8/W;
Vbank8=sqrt(r8*g*sqrt(n^2-1));
ta8=arc8/Vbank8;

t=t+ta8;
```

P. Right Turn #9

```
r9=215; c9=172.5;
bank9=80; %degrees
loc9=acos((c9^2-2*r9^2)./(-2*r9^2));
arc9=loc9*r9;
bank9=bank9*pi()/180;
liftt9=W./cos(bank9);
n=liftt9/W;
Vbank9=sqrt(r9*g*sqrt(n^2-1));
ta9=arc9/Vbank9;

t=t+ta9;
```

Q. Left Turn #10

```
r10=180; c10=200;
bank10=80; %degrees
loc10=acos((c10^2-2*r10^2)./(-2*r10^2));
arc10=loc10*r10;
bank10=bank10*pi()/180;
liftt10=W./cos(bank10);
n=liftt10/W;
Vbank10=sqrt(r10*g*sqrt(n^2-1));
ta10=arc10/Vbank10;

t=t+ta10;
```

R. Output Run Time

```
fprintf('The final runtime is %f seconds',t);
```

The final runtime is 49.208609 seconds

Appendix B: Vortex Lattice Method

```
clc
clear all

%Vortex Lattice Method for AE-429
%Andrew Kail, Sydney Fears, Eric Kirchoff, Chad Sutton
%May 2nd, 2011
```

Initial Input:

```
sweep1=21.3;% (Degrees)
sweep1r=sweep1*pi()/180;
b=8;
cr=1.75; ct=0.75;
lambda=ct/cr;
AR1=2*b./(cr+ct);
S=0.5*b*(cr+ct);

sweep3r=atan(tan(sweep1r)-4./(AR1)*(2/4)*((1-lambda)./(1+lambda)));

%j=input('Number of panels? \n');
dy=0.1; % Panel size in terms of b
j=b/dy;
dy2=dy/b;
%Vortex Bounds & control points in terms of b
bounds=zeros(j,7);

for i=1:1:j;
   bounds(i,1)=i;
   %Control points
   bounds(i,3)=0.5*dy2+(i-1)*dy2;
   bounds(i,2)=cr/b*3/4+tan(sweep3r)*bounds(i,3);
   %End points
   bounds(i,5)=(i-1)*dy2;
   bounds(i,4)=cr/b*1/4+bounds(i,5)*tan(sweep1r);
   bounds(i,7)=(i)*dy2;
   bounds(i,6)=cr/b*1/4+bounds(i,7)*tan(sweep1r);
end

flow=zeros(j,j);

for k=1:1:j % panels
   for i=1:1:j % vortex summation at panel k

      s1=(1/((bounds(k,2)-(bounds(i,4)))*(bounds(k,3)-(bounds(i,7)))- (bounds(k,2)-(bounds(i,6)))*(bounds(k,3)-(bounds(i,5)))));
      s2=((((bounds(i,6)-bounds(i,4))*(bounds(k,2)-bounds(i,4)))+(bounds(i,7)-bounds(i,5))*(bounds(k,3)-bounds(i,5)))  / sqrt(
(bounds(k,2)-bounds(i,4))^2+ (bounds(k,3)-bounds(i,5))^2));
      s3=((((bounds(i,6)-bounds(i,4))*(bounds(k,2)-bounds(i,6)))+(bounds(i,7)-bounds(i,5))*(bounds(k,3)-bounds(i,7)))  / sqrt(
(bounds(k,2)-bounds(i,6))^2+ (bounds(k,3)-bounds(i,7))^2));
      s4=1.0/(bounds(i,5)-bounds(k,3))*(1+ (bounds(k,2)-bounds(i,4))/sqrt( (bounds(k,2)-bounds(i,4))^2+ (bounds(k,3)-
bounds(i,5))^2));
      s5=1.0/(bounds(i,7)-bounds(k,3))*(1+ (bounds(k,2)-bounds(i,6))/sqrt( (bounds(k,2)-bounds(i,6))^2+ (bounds(k,3)-
bounds(i,7))^2));

      starboard=s1*(s2-s3)+s4-s5;

      p1=(1/((bounds(k,2)-(bounds(i,4)))*(bounds(k,3)+(bounds(i,7)))- (bounds(k,2)-(bounds(i,6)))*(bounds(k,3)+(bounds(i,5)))));
      p2=((((bounds(i,6)-bounds(i,4))*(bounds(k,2)-bounds(i,4)))+(-bounds(i,7)+bounds(i,5))*(bounds(k,3)+bounds(i,5)))  / sqrt(
(bounds(k,2)-bounds(i,4))^2+ (bounds(k,3)+bounds(i,5))^2));
```

```
        p3=((((bounds(i,6)-bounds(i,4))*(bounds(k,2)-bounds(i,6)))+(-bounds(i,7)+bounds(i,5))*(bounds(k,3)+bounds(i,7)))  / sqrt(
(bounds(k,2)-bounds(i,6))^2+ (bounds(k,3)+bounds(i,7))^2));
        p4=1.0/(-bounds(i,5)-bounds(k,3))*(1+ (bounds(k,2)-bounds(i,4))/sqrt( (bounds(k,2)-bounds(i,4))^2+
(bounds(k,3)+bounds(i,5))^2));
        p5=1.0/(-bounds(i,7)-bounds(k,3))*(1+ (bounds(k,2)-bounds(i,6))/sqrt( (bounds(k,2)-bounds(i,6))^2+
(bounds(k,3)+bounds(i,7))^2));

        port=p1*(p2-p3)+p4-p5;

        w=starboard-port;
        flow(k,i)=w;
    end
end

for i=1:1:j
    ones(i,1)=-1;
end

streamlines=flow\ones;

sum=0;
for i=1:1:j
    sum=sum+ streamlines(i,1);
end

Cl=b^2*2*pi()*sum*dy./S;

x=0:0.5:15;
y=Cl*pi()/180*x;
subplot(1,2,1)
plot(x,y)
xlabel('Angle of Attack (degrees)')
ylabel('Cl')
```

S. Lift distribution

```
vmax=110; %m/s

rho=1.225;%density
j2=2*j;
for i=1:1:j2
    if i <= j
        clift(i)=streamlines(j-i+1);

    else
        clift(i)=streamlines(i-j);
    end

end

lift=clift*rho*vmax;
dx=b/j;
xlift=-b:dx:b-dx;
subplot(1,2,2)
plot(xlift,lift)
plot(xlift,lift)
xlabel('Wingspan (meters)')
ylabel('Lift (newtons)')
```
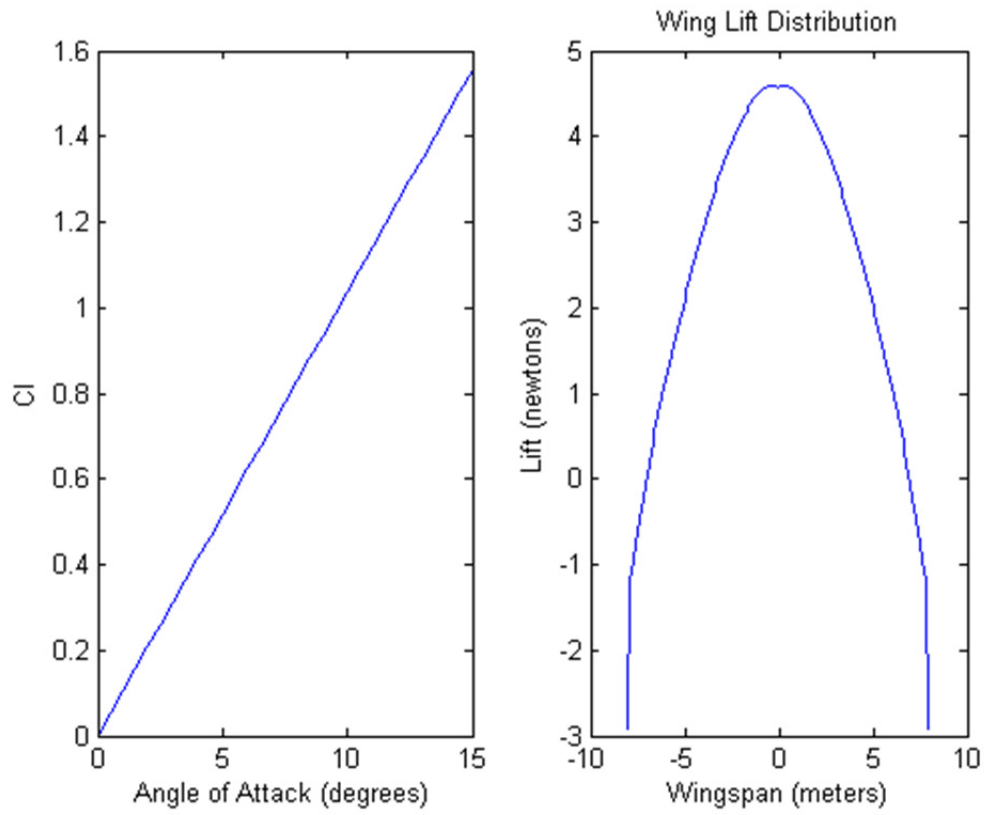
title('Wing Lift Distribution')

T. excel export
        xlswrite('vlmdata.xls',lift)